JGR Earth Surface

RESEARCH ARTICLE
10.1029/2025JF009008

Calibrated Granular-Flow PIV From DEM Simulations: Flow-Substrate Dynamics in Flows With Fixed and Erodible Substrates, Modeling, and Field Implications

Symeon Makris[1,2], **Eric C. P. Breard**[2,3], **and Eliza S. Calder**[2]

[1]British Geological Survey (BGS), The Lyell Centre, Edinburgh, UK, [2]School of Geosciences, University of Edinburgh, Edinburgh, UK, [3]Department of Earth Sciences, University of Oregon, Eugene, OR, USA

Key Points:

- PIV underestimates granular temperature by ~34%; discrete element method-based calibration corrects this bias for accurate experimental flow analysis
- Flows' basal agitation is strong on fixed beds; erodible beds transmit motion to the substrate, with a shifting, transient flow–bed boundary
- Model—experiment mismatch shows erosion laws miss transient bulking–debulking, key for interpreting basal contacts in field deposits

Supporting Information:

Supporting Information may be found in the online version of this article.

Correspondence to:

S. Makris,
smakr@bgs.ac.uk

Citation:

Makris, S., Breard, E. C. P., & Calder, E. S. (2026). Calibrated granular-flow PIV from DEM simulations: Flow-substrate dynamics in flows with fixed and erodible substrates, modeling, and field implications. *Journal of Geophysical Research: Earth Surface*, *131*, e2025JF009008. https://doi.org/10.1029/2025JF009008

Received 12 NOV 2025
Accepted 25 MAR 2026

Author Contributions:

Conceptualization: Symeon Makris, Eric C. P. Breard, Eliza S. Calder
Formal analysis: Symeon Makris, Eric C. P. Breard
Funding acquisition: Eric C. P. Breard, Eliza S. Calder
Investigation: Symeon Makris, Eric C. P. Breard, Eliza S. Calder
Methodology: Symeon Makris, Eric C. P. Breard
Project administration: Eliza S. Calder
Resources: Eric C. P. Breard, Eliza S. Calder

Abstract Granular flows are central to geophysical and industrial processes, yet their internal properties remain difficult to quantify. Understanding how energy and momentum are exchanged at the flow–substrate boundary is key to predicting their erosion and mobility. Here, we assess the accuracy of particle image velocimetry (PIV) in resolving velocity and granular temperature (T) in analog granular flows using like-for-like comparisons with discrete element method simulations. Synthetic image sequences from simulations reveal that PIV systematically underestimates T by ~34% owing to Eulerian spatial averaging. Applying this correction factor enables accurate quantification of T within stated uncertainties. This calibrated approach integrates laboratory, numerical, and field perspectives, offering new constraints on granular rheology and flow–bed coupling. Applying this calibrated workflow to analog flows over fixed and erodible beds reveals fundamental behavioral contrasts. Fixed rough beds exhibit basal T spikes caused by intense shear and grain interlocking, whereas erodible substrates transmit momentum and T into the substrate, producing velocity profiles that rise exponentially within the substrate. The flow–substrate interface is dynamic, oscillating and alternating erosion and deposition. These results identify T as a key link between local and non-local rheology: agitation within the flow can propagate, weaken the substrate, and control entrainment. Frame-by-frame velocity-based boundary tracking reveals that standard erosion–deposition laws in depth-averaged models fail to reproduce even simple experiments, highlighting the need for revision, especially for steep, mobile beds. Findings allow the observation and tracking of the fluctuating flow-substrate interface observed in the deposits of many geophysical flows.

Plain Language Summary Granular materials, such as sand or volcanic ash, are transported in rapid flows during landslides, volcanic eruptions, or industrial processes, yet their internal dynamics remain difficult to measure. Understanding how energy and momentum are exchanged at the flow–substrate boundary is key to predicting their erosion, mobility, and runout. Here, we used computer simulations and laboratory experiments to test how accurately particle image velocimetry (PIV), a technique that tracks motion, captures flow dynamics. PIV was found to underestimate small, fast grain motions defined as granular temperature (T), a measure of internal agitation. By comparing PIV measurements with discrete element method simulations, where every particle's motion is known, we derived a correction factor showing that true T values are about 1.34 times higher than PIV-derived. Measurements reveal strong basal agitation and a distinct T spike over fixed beds, while erodible beds transmitted motion deeper and displayed a shifting flow-substrate interface with alternating erosion, and deposition. The calibrated workflow demonstrates that existing erosion–deposition laws implemented in models fail to reproduce even simple experiments. The approach unites laboratory, numerical, and field perspectives, allows the observation of the flow-substrate boundary which has been suggested as unstable in natural deposits.

1. Introduction

Granular flow dynamics govern the propagation of a wide range of hazardous geophysical phenomena, from rapid rock and debris avalanches to pyroclastic density currents (e.g., Breard et al., 2019; Iverson & Vallance, 2001; Makris, Roverato, Dávila-Harris et al., 2023; Tai & Kuo, 2008). Also, fluid mediated flow dynamics are controlled not only by the fluid forces but also by grain–grain interactions and momentum exchange (e.g., Bagnold, 1956; Pähtz & Durán, 2020). Beyond natural flows, granular dynamics underpin many industrial operations such as powder mixing, transport, and conveying (e.g., Albaraki & Antony, 2014; Gollin et al., 2017;

Supervision: Eric C. P. Breard, Eliza S. Calder
Visualization: Symeon Makris, Eric C. P. Breard
Writing – original draft: Symeon Makris
Writing – review & editing: Eric C. P. Breard, Eliza S. Calder

Ostendorf & Schwedes, 2005; Sielamowicz et al., 2011). For both natural and industrial granular flows the accurate characterization of their dynamics presents significant challenges due to their complex and highly transient nature. Predicting their mobility and runout requires understanding the energy and momentum exchange at the flow–substrate boundary, where erosion and deposition regulate the basal conditions. Yet this interface remains one of the least constrained aspects of granular flow dynamics.

In granular flows, particles interact through collisions, leading to fluctuations in their velocities around the Reynolds-averaged mean flow velocity (Sanvitale & Bowman, 2016; Sarno, Carravetta, et al., 2018). These fluctuations are analogous to random motions in molecular gases as described by kinetic theory (Campbell, 1990). The granular temperature (T), defined as the specific kinetic energy of these velocity fluctuations, quantifies internal agitation within a granular medium (Brilliantov & Pöschel, 2004; Jesuthasan et al., 2006; Ogawa, 1978). As a measure of the energy exchange, T ($\mathrm{m}^2\mathrm{s}^{-2}$) offers insight into momentum transfer and dissipation. Increasing T indicates a transition from a quasistatic, friction-dominated regime to a collisional regime characterized by short-lived contacts and dilation, where the flow behaves similarly to a molecular gas (Brilliantov & Pöschel, 2010; Campbell, 1990, 2005; Drake, 1991; Johnson et al., 2016). These flow regimes differ in energy dissipation patterns and mobility. Consequently, T is a critical diagnostic for classifying flow regimes and understanding internal agitation and rheology (Campbell, 1990; Iverson, 1997; Makris et al., 2024; Makris, Roverato, Lomoschitz, et al., 2023; Ogawa, 1978; Sanvitale & Bowman, 2016; Straub, 1996).

In rheological modeling, the widely used $\mu(I)$ framework describes the effective friction coefficient μ as a function of the dimensionless shear rate, the inertial number I (Breard et al., 2024; GDR MiDi, 2004; Jop et al., 2006; Kim & Kamrin, 2020). While successful in capturing steady, dense granular flows, the $\mu(I)$ model lacks explicit treatment of grain-scale energy fluctuations. Recent studies suggest that incorporating T as an additional state variable enhances predictive capability in non-local and transient regimes (Breard et al., 2024; Kim & Kamrin, 2020; Zrelak et al., 2024). For example, Kim and Kamrin (2020) illustrated that augmenting the $\mu(I)$ model with T improved predictions across diverse flow geometries, while Breard et al. (2024) proposed a unified model coupling $\mu(I)$ and T to better capture transitions between dense and collisional regimes. Constraining how T evolves and dissipates within granular masses remains central to advancing the understanding and modeling granular flows. Quantifying T provides a means to evaluate how agitation generated in one region of a flow can propagate, weaken underlying material, and trigger entrainment. This study therefore focuses on evaluating a method for the effective measurement of velocity and T profiles in flows over fixed and erodible beds in controlled experiments. The measurements allowed by this method enable the examination of the processes and dynamics of the flow-substrate interface. Furthermore, observations and measurements at the particle-scale resolution provide a mechanistic framework for monitoring the flow-substrate interface and testing erosion–deposition laws and interpreting basal contacts preserved in natural deposits.

Particle image velocimetry (PIV) has emerged as a widely used technique to quantify velocity fields (e.g., Zuccarini et al., 2025) and T (e.g., Sarno, Carravetta, et al., 2018; Sanvitale & Bowman, 2016) in granular flow experiments. The potential for PIV to be applied to suboptimal footage for the characterization of natural geophysical flows has been explored (Zuccarini et al., 2025), nonetheless, the accuracy and precision of this technique has not been definitively verified or calibrated against flows with independently quantified properties. Assessing the reliability of PIV is therefore crucial for both laboratory studies and potential applications to the monitoring of natural and industrial mass flows.

This study evaluates the potential of PIV for measuring experimental granular flow properties velocity and T, through the analysis of flow-lateral high speed imaging. Specifically, the multi-pass window deformation method of the open-source *PIVlab* code developed in Thielicke and Stamhuis (2014) and Thielicke and Stamhuis (2019) is used and evaluated. The *PIVlab* code has been applied to experimental granular flows in various studies (e.g. Gollin et al., 2017; Jiang & Towhata, 2013; Sarno, Carleo, et al., 2018; Sarno, Carravetta, et al., 2018; Thielicke & Sonntag, 2021). The code represents a state-of-the-art multi-pass window deformation algorithm capability, which offers significant advantages and improvement over single-pass PIV. The capability of utilizing interrogation windows (IWs) with consecutively smaller areas limits the loss-of-pair errors which typically result when a single IW is too small (Sarno, Carravetta, et al., 2018). To eliminate this error, larger IWs would have to be used in the single-pass approach. However, the four passes available in *PIVlab* allows for progressively smaller IWs to increase the measurement resolution without compromising quality. PIVlab's multi-pass capabilities have proved superior to other codes for the measurement of T (Sarno, Carravetta, et al., 2018).

The calculation of T from PIV measurements is affected by two sources of known error additional to those affecting bulk-averaged velocity measurements: (a) Using PIV for the estimation of second order statistics such as the velocity variance and T involves quadratic operators. In contrast to average operators (e.g., mean velocity), which dampen the effect of random errors in instantaneous velocity, quadratic operators amplify them (Sarno, Carravetta, et al., 2018). (b) Since PIV measurements are a space-averaged bulk measurement of displacement within each Eulerian IW, the instantaneous velocities are smoothed by such measurement, and thus maximum velocity fluctuations are not captured. This inevitably causes a systematic underestimation of both velocity variance and T. Based on a statistical geometrical argument Reynolds et al. (2008), suggest that the underestimation is systematic and correlated to the size of the IW. However, contrary to that, the correlation has been found inconsistent by Sarno, Carravetta, et al. (2018) who observed that the correlation is not as predicted for the multi-pass approach. The T estimations do not increase with IW size as predicted to compensate for the underestimation. One aim of this study is therefore to quantify PIV accuracy and precision for velocity and T, and to determine how PIV can most effectively capture granular flow dynamics.

The aim of this study was to examine the dynamics at the flow-substrate interface, their transmission higher up in the flows, and to develop a method which would allow the accurate and effective measurement of particle-scale processes. Therefore, this study initially evaluates the most effective and accurate use of PIV to measure the dynamics of granular flows. To achieve this, discrete element method (DEM) simulations generate three-dimensional granular flows with fully resolved particle kinematics, allowing direct computation of velocity and T. DEM modeling is a particle-based numerical approach that resolves the motion and interaction of individual grains through contact mechanics (Cundall & Strack, 1979; O'Sullivan, 2011; Zhu et al., 2008). By computing particle trajectories and velocities directly in three dimensions, DEM provides access to fully resolved kinematics and allows T to be calculated. As such, DEM simulations provide a physically consistent benchmark against which experimental PIV measurements can be evaluated. Two-dimensional image sequences derived from the simulations are then analyzed using PIV to measure instantaneous velocity in the x and z dimensions. The comparison of the simulation data with the PIV analysis of the same simulation outputs allows for the quantification of PIV systematic bias and the derivation of a robust correction factor for the estimation of T.

The calibrated PIV workflow is then applied to analog experiments to examine the flow-substrate interface. The first objective was to evaluate the different mechanisms between fixed rough substrates and erodible substrates. We investigate how basal boundary conditions influence velocity profiles, T distribution, and substrate entrainment, key factors in determining flow regime transitions and mobility. Flows over fixed and erodible beds differ fundamentally: fixed beds generate basal agitation through grain interlocking, while erodible beds dissipate energy into the substrate, altering entrainment and deposition behavior. For erodible substrates, the second objective was to use the calibrated methodology for frame-by-frame identification of the evolving flow–substrate boundary and tracking of erosion and deposition patterns. By directly measuring these processes, we provide an empirical basis for evaluating erosion formulations in depth-averaged models and for proposing the mechanisms responsible for the behavior observed in the deposits of natural mass flows, which was the third objective.

Therefore, in Section 2 we describe the experimental setup, DEM simulations, and PIV methodology. Section 3 presents the outputs of the numerical simulations, calibration of PIV against DEM data and the derivation of a correction factor for T, followed by observations from the analog experiments. The first part of Section 4 evaluates the performance and limitations of the calibrated PIV workflow. We then examine the dynamics of granular flows over fixed and erodible substrates. Finally, we discuss the broader implications of these findings for the formulation of erosion–deposition laws in depth-averaged models and for interpreting basal contacts in natural deposits.

2. Methods

2.1. Analog Granular Flows on a Rough Substrate

Analog experiments were carried out to examine the dynamics of granular flows propagating over a fixed rough substrate at different slope inclinations. The experiments were carried out in the flume facility in the Geophysical Flow Lab at the School of Geosciences, University of Edinburgh (Figure 1a). The flume has a length of 3.0 m and a width of 0.3 m. The experimental flows were composed of natural-shaped sand particles with d_{43} (Breard et al., 2020; Gu et al., 2016) diameter of 875.4 µm, and a d_{32} diameter (Breard et al., 2019) of 814.7 µm (Text S1 in Supporting Information S1). The fixed rough substrate was prepared by adhering a single layer of sand to the

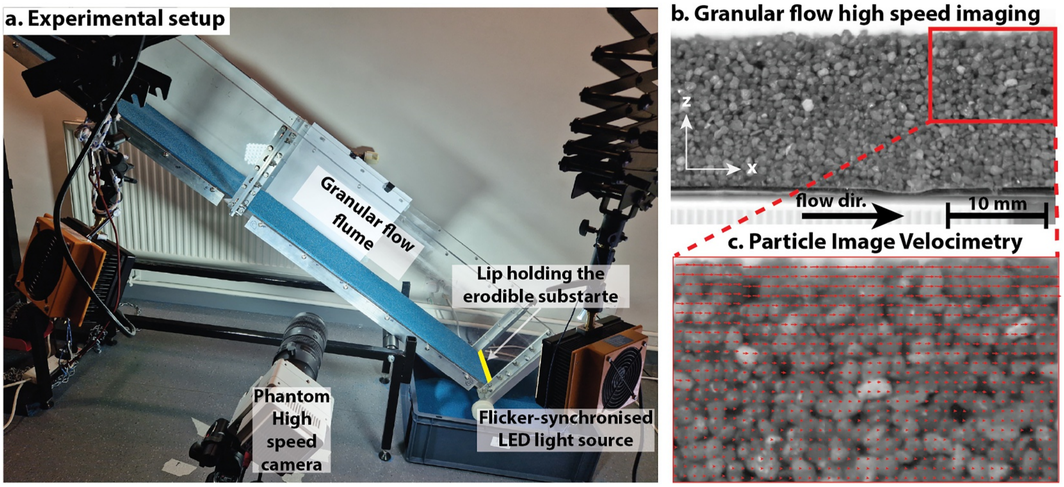

Figure 1. The flume setup hosting the analog granular flows. (a) Variable inclination flume with imaging system, rough substrate. The flume has the potential of adding a lip to hold an erodible substrate for experimental flows to propagate on instead of the fixed rough substrate. (b) Example of one frame of the imaging sequence of the granular flows. (c) Eulerian particle image velocimetry vectors indicating instantaneous velocity for each of the interrogation windows that the image is subdivided into. These fields are then analyzed to calculate the flow dynamics such as velocity and granular temperature profiles.

bottom of the flume. This sand had a d_{43} diameter of 1,063.5 μm (Text S1 in Supporting Information S1), and a d_{32} diameter of 983.0 μm. The granular material was held in a release box at the top of the flume and the flow was initiated by the rapid removal of a sliding gate. A second gate controlled flow discharge (Text S1 in Supporting Information S1), with a constant opening of 50 mm. Flows were generated at 36°, 38°, 40°, and 42° flume slope inclinations.

The flows were imaged at 1,800 Hz at a resolution of 2,048 × 1,152 pixels (Figure 1b) using a *Phantom VEO* 440 high-speed camera. Flicker synchronization between the LED lights and the camera ensured uniform lighting in all frames. This footage was calibrated for lens distortion using images of a grid with identical squares of known dimensions. For the analysis of the flows on a fixed substrate, a period of 3 s was determined when the flow was steady. This required a pilot analysis to assess the average velocity and thickness of the flows during their entire propagation. Adapting the method of Arran et al. (2024), the flow period is subdivided into 0.25 s intervals, and flows are considered to have reached a steady state at the end of an interval over which the mean flow velocity and standard deviation of the velocity vectors is within 10% of the previous interval. Note that the threshold here is higher than the 5% of Arran et al. (2024) due to the added complexity of the irregular shapes of the sand particles (not spherical glass beads), resulting in more transient flows. We also ensured that the flow height does not vary by more than 10% in consecutive periods. In Arran et al. (2024), a duration of 1 s from each of these flows is used for the analysis. We increase the time sampled to 3 s in this case to limit the effect of outliers in the velocity measurements. We define x downslope (flow-parallel), z base-normal (flow height), and y cross-slope.

2.2. Analog Granular Flows on Erodible Substrate

To examine the transmission of T from the flow to a substrate, experiments of flows with sand propagating over an erodible substrate of the same material were performed. The opening of the gate was varied between 20 and 100 mm to generate flows with different thicknesses and dynamics. The substrate was created by installing a lip at the end of the flume holding a 150-mm-high pile of material on the slope. The slope inclination was constant at 31° (Figure 1a). These flows were more temporally transient and generally did not develop into stable flows for periods over half a second to allow comparison between them. Therefore, their velocity, T and interaction with the substrate are evaluated and visualized through time rather than treated as time-averaged stable processes.

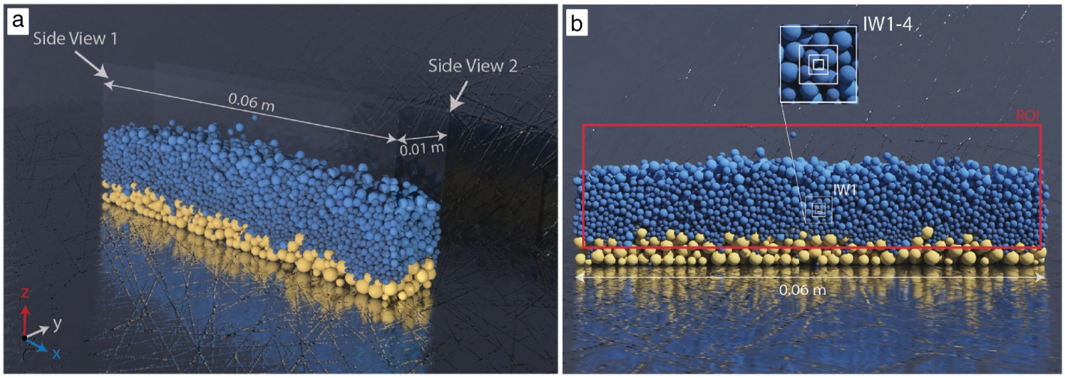

Figure 2. Discrete element method simulations of granular flows. (a) Three-dimensional rendering of the simulations illustrating the dimensions and the confining walls and both sides of the simulated flume (SV1 and SV2) where image sequences and flow properties were exported from the simulations; (b) Imaging from side view 1 (SV1), illustrating particle arrangements and the relative size of interrogation windows used for the particle image velocimetry analysis.

2.3. Generating Discrete Element Method (DEM) Granular Flows for Particle Image Velocimetry (PIV) Calibration

To assess the accuracy of PIV results and permit their calibration, DEM simulations of free surface granular flows were generated with known properties with which PIV measurements could be compared. The simulated flows propagated on an inclined rough surface at different slope inclinations: 36°, 38°, and 40°. The simulations were generated with the *MFiX* open-source code developed by the US Department of Energy's National Energy Technology Laboratory (NETL) (Syamlal et al., 2016). The conditions of these simulations and exported footage were as much as possible similar to the analog experiments described above, in order to ensure transferability of the calibration. The flows propagated on a randomly generated, fixed substrate composed of particles of a coarser particle size distribution than the particles in the flow. The size distribution for the simulated granular material was imported from the histogram of the particle size analysis of the sand used in the analog experiments. The substrate was not identical across the simulated domain, resulting in minor natural variations between the two sides of the flow and causing slight differences in the data extracted from the front and back views. This allowed for the generation of image sequences from either side of the simulated flume, called side view 1 (SV1) and side view 2 (SV2) (Figure 2a). Analysis of either side expanded the data set allowing the accuracy of PIV to be evaluated. Due to the particles in the simulations being spherical, and the experimental material more angular, an arbitrary rotational friction was added to generate a rolling resistance in the simulations to force the spheres to decrease their velocity closer to the velocities observed in the analog experiments. Nevertheless, the similarity of the velocity is not highly relevant since comparison between the experimental and simulated flows was not the principal aim. Instead, the aim is to generate a numerically determined sequence of flow image sequences with numerically constrained parameters which could be processed with PIV to allow independent determination of the flow characteristics for PIV calibration. The DEM simulations are used solely to quantify systematic PIV measurement bias arising from spatial averaging, rather than to reproduce material-specific flow behavior; the correction therefore addresses methodological underestimation of velocity fluctuations and is independent of particle shape–dependent rheology.

The numerical simulations were used to generate synthetic image sequences to which PIV analysis could be independently applied (Figure 2). The image sequences were captured over 3-s periods during which the flows were steady. In this case, a steady flow is defined based on the thickness of the flow and its mean velocity and standard deviation. For the numerical simulations, the flows accelerated until they reached a steady mean velocity and velocity standard deviation varying <5% between consecutive 0.25-s periods (Arran et al., 2024). The image sequences were exported at a frame rate of 1,800 Hz and a resolution of 0.04 mm/pixel to match the specifications of the footage captured from the analog experiments with an equivalent number of pixels per particle. The use of high resolution and frame rate is vital for the PIV methodology, since PIV involves a random error of ~0.02 pixels/frame (Thielicke & Stamhuis, 2014) which is therefore greatest for velocity measurements at coarser resolutions and less frequent sampling rates. To ensure that the sampling frequency of 1,800 Hz was sufficient to reflect the vibration of the particles, one of the simulated flows was resampled at 18,000 Hz (one order of magnitude greater) so that the sampling rate was sufficiently high enough to capture the velocity fluctuations (Figure S2 in Supporting Information S1). The synthetic image sequences were also used to assess the most effective PIV setting configuration (number of passes and IW size) in terms of accuracy and precision, as described in Section 3.2.1. For comparison of different configurations, a smaller subsample of 150 frames of the 38° simulations were analyzed with various PIV numbers of passes and IW sizes.

2.4. Particle Image Velocimetry (PIV) Analysis

Since PIV can only be applied to side views of experimental granular flows through transparent walls, only particles visible in the videos are analyzed. From the simulations, lateral image sequences were exported from the regions adjacent to the confining wall (Figure S3 in Supporting Information S1), providing direct analogs to the experimental videos. In the analog experiments, it was visually estimated that the depth of the flow visible in the videos was equal to 2 median particle diameters (d_{43}). In the numerical simulations the optimal visualization optics, higher agitation levels and perfect roundness of the particles allow ease of particle observation further from the flow margin. To ensure consistency with the experimental conditions, and because the effective depth of observation could not be determined precisely, only particles within a region extending $2d_{43}$ from the wall were included in the exported simulation sequences.

The PIVlab algorithm divides each frame of the provided image sequence into partially overlapping IWs for Eulerian examination (Figure 1c). Between consecutive images, the cross-correlation of the image intensity fields in identified groups of pixels is evaluated to determine the most likely displacement in each IW (Raffel et al., 2007; Thielicke & Stamhuis, 2014). The Fast Fourier Transform interpolation algorithm of PIVlab is employed to solve the optimization in the frequency domain. The window deformation algorithm employs nine-point bilinear interpolation for the IW reconstruction. For sub-pixel accuracy, a three-point Gaussian interpolation independently solves for the vertical and horizontal components of the displacement (2×3-point interpolation, e.g., Westerweel, 1993). A discussion of PIV theory and PIVlab features relevant to the tracking of granular flows is provided by Sarno, Carravetta, et al. (2018). Displacement of the particles in the y-direction (i.e., aligned with the flow width, wall-to-wall) is inevitably not accounted for.

Since the *PIVlab* algorithm permits a maximum of four passes, subsequent IW passes were progressively decreased in size to increase the accuracy of the measurements and limit the smoothing effect of averaging the displacement in larger IWs. IW overlap was kept constant at 50%. In order to avoid loss-of-pair errors the largest IW is advised to be at least 4 times greater than the maximum particle size (e.g., Keane & Adrian, 1992), as well as 4 times greater than the mean particle displacement distance in each frame (Keane & Adrian, 1990). Each subsequent pass determines the displacement within the new smaller IW and adds it to the displacement detected in the previous larger IW (Thielicke & Stamhuis, 2014). A number of studies suggest that the smallest IW in the sequence should not be <5–8 pixels (Gollin et al., 2017; Sarno, Carravetta, et al., 2018; Taylor-Noonan et al., 2021). Note that in videos from experimental granular flows the particles are irregular and non-identical, with distinct shapes and textures. These characteristics enhance the ability of PIV algorithms to identify patterns and thereby reduce measurement noise (Eckart et al., 2003; Taylor-Noonan et al., 2021), compared with the results obtained from our calibration tests using simulated image sequences of identical perfect spheres with no unique texture.

2.5. Velocity Measurements and Secondary Statistics Calculation

For the numerically simulated flows, the instantaneous velocities of the particles at each time interval are exported from the 3D DEM simulations. The average profile of the simulated granular flows for the x, y, and z components of the velocity were then computed, along with the corresponding velocity variance of the velocity and T profiles. Synthetic image sequences were generated from the simulations in *Paraview*® v5.11.1, and processed in *PIVlab* to independently measure instantaneous velocities in the x and z directions. From these variance and T profiles could be recalculated and compared to the results from the numerical simulations. Since PIV from the side of the flow can only track the movement of particles in the x and z directions (Figure 1b), all the T measurements calculated from PIV (T_{PIV}) are 2D, and exclude the y direction (Figure 2). Each flow is divided vertically at height intervals of 1 d_{43}. At each height interval velocity vectors are grouped for the particle population in that area, allowing the calculation of the velocity and T_{PIV} values which constitute the profiles. For steady flows from numerical simulations and analog experiments on a fixed rough substrate, time-averaged velocity and T_{PIV} profiles were generated.

In the case of numerical simulations, where the three components of the instantaneous velocity are available and only the translational specific kinetic energy is considered, the volume-weighted $T_{\mathrm{MFiX^{3D}}}$ is expressed by the equation:

$$T_{\mathrm{MFiX^{3D}}} = \frac{1}{3}\sum_{i=1}^{3}\frac{\sum V\left(u_i' - \langle u_i'\rangle\right)^2}{\sum VN} \tag{1}$$

where V represents the volume of each particle in each flow height interval, N is the number of velocity observations, and u_i' is the i-component (u_x', u_y', u_z') of the instantaneous velocity. The angle brackets $\langle\rangle$ denote an ensemble-averaging operator applied independently to each height interval. Because all particles have the same density, volume is used as a proxy for mass. Assuming the system is steady and ergodic, the ensemble average can be approximated by the time variance of the instantaneous velocities (e.g., Sarno, Carleo, et al., 2018; Sarno, Carravetta, et al., 2018). Both velocity variance and T are expressed in $\mathrm{m}^2\ \mathrm{s}^{-2}$.

The $T_{\mathrm{MFiX^{2D}}}$ term only considers the x and z velocity components and is therefore equivalent to T_{PIV}, enabling direct comparison. In this case, u_x' and u_z' are the only components included in the equation:

$$T_{\mathrm{MFiX^{2D}}} = \frac{1}{2}\sum_{i=1}^{2}\frac{\sum V\left(u_i' - \langle u_i'\rangle\right)^2}{\sum VN} \tag{2}$$

Since the y-component of the velocity cannot be observed, previous studies (e.g., Jesuthasan et al., 2006; Sarno, Carravetta, et al., 2018) have assumed that the fluctuations in the y-component of the velocity can be approximated and assumed equal in magnitude to the z component. Although this assumption cannot be tested in the analog experiments, the numerical simulations suggest a deviation, the variance of the z-component is consistently higher. This could be a result of the specific conditions of the simulated granular flows. However, to avoid additional uncertainties, the equation used by Sanvitale and Bowman (2016) and Gollin et al. (2017), which only considers the u_x' and u_z' is adopted here:

$$T_{PIV} = \frac{1}{2}\left(\left\langle v_x'^2 + v_z'^2\right\rangle\right) \tag{3}$$

where v_x' is the velocity variance/fluctuation in the x direction and v_z' in the z dimension (Figure 1b). In the case of T_{PIV}, the equation does not need to be weighted by the area/volume of individual particles, as larger particles will be proportionally sampled by more IWs.

For both the simulated and the experimental flows on a fixed rough substrate, the flows achieve a steady state. The velocity profiles that are presented to describe that state were obtained by temporally and spatially averaging all velocity vectors across all frames within the time range defined as steady. For T calculations, the variance represents the sum of the differences between the velocity in each height interval and the temporal average for that height interval, such that:

$$v_i' = \frac{1}{N}\sum\left(u_i' - \langle u_i'\rangle\right) \tag{4}$$

where $\langle u_i'\rangle$ is averaged between all frames in the steady-state period. For more transient flows on an erodible substrate, which did not become steady, the variance was calculated instantaneously. This was done within a single frame by comparing the velocity variance of the particles in a narrow region ($10d_{43}$) of the same frame. The particles in this area are assumed to flow under the same regime at each imaging interval.

Experimental flows over an erodible substrate were not steady, therefore, their dynamics are not time-averaged. Instead, their transient nature is represented on spatio-temporal plots. Even though not steady, their velocity profiles can consistently be divided into four regions (Figure 3): (a) The true substrate comprises the basal

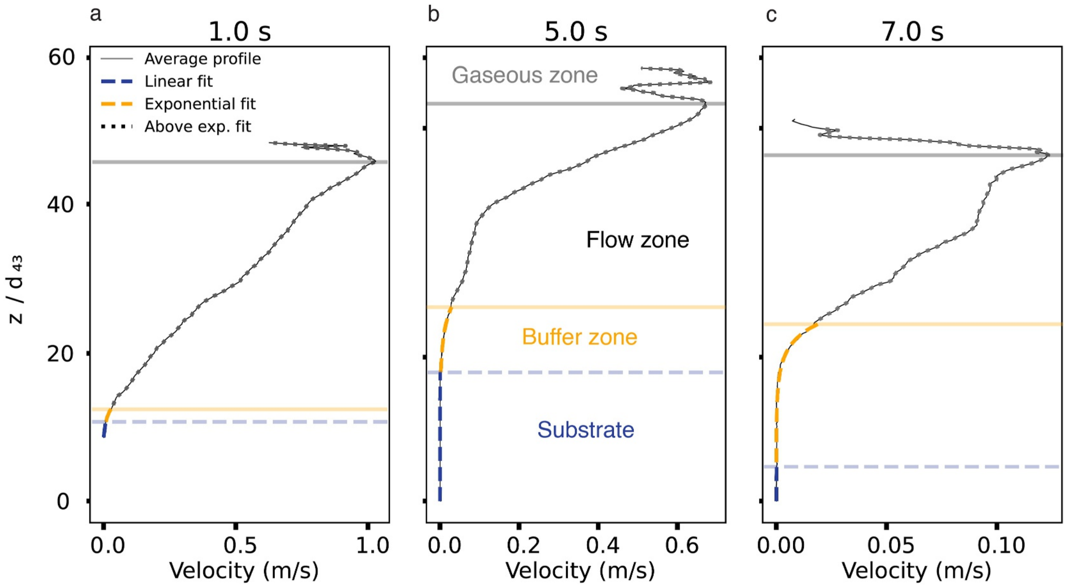

Figure 3. Definition of velocity profile zones for granular flows on an erodible substrate. Example profiles from the flow with a 100 mm gate opening at: (a) 1 s, (b) 5 s, (c) 7 s. The profiles illustrate the division into four distinct velocity profile regions: true substrate (linear relationship fitted from the base), buffer zone (exponential velocity increase), actively shearing flow zone, and gaseous zone (excluded from analysis).

material that remains unaffected by the flow above. This zone was identified by fitting a linear relationship from the stationary base of the flume upward, until the point where the measured velocity diverged from this line by more than the random error threshold of PIVlab. (b) Immediately above is the buffer zone, where velocity increases exponentially. This region consists of material transitioning from the static substrate to the actively shearing flow, as described by Richard et al. (2020) and GDR MiDi (2004). The upper limit of this zone is marked where the profile departs from the exponential trend beyond the PIVlab random error threshold. (c) The region above the buffer zone is the flow zone, whose profile varies throughout the flow. The maximum velocity within the profile occurs inside this flow zone. (d) Above it, saltating particles detached from the main flow are increasingly influenced by air drag and collisions with the flow surface, resulting in lower velocities. These particles form the gaseous zone, which is excluded from analysis in this study. The specific aim was to identify the depth to which velocity and T are transmitted and the thickness of the true flow. Therefore, the definitions of the static substrate and buffer zone used here differ from those of the creep zone described in other studies (e.g., Crassous et al., 2008; Jerolmack & Daniels, 2019; Komatsu et al., 2001; Richard et al., 2020). Under optimal conditions, the theoretical bias error of the window deformation of PIVlab is <0.005 pixels and the random error is <0.02 pixels. Therefore, a threshold of 0.025 pixels frame^{-1} was adopted to define the flow–substrate boundary, since lower velocities cannot be measured reliably.

3. Results

3.1. DEM Numerical Simulations

DEM numerical simulations of granular flows were carried out for three slope inclinations. The velocity, $T_{\mathrm{MFiX}^{2D}}$, and $T_{\mathrm{MFiX}^{3D}}$ were calculated along either side of the confining walls. These values were obtained directly from the DEM simulation outputs. In addition, flume-averaged values, including all particles in the simulation domain, were computed to examine lateral heterogeneity (Figure 4). The properties of each particle, including position, velocity components and diameter were exported for each time step (i.e., frame). For clarity, only the results from SV2 are visualized in subsequent plots; the remaining data are provided in Figure S4 in Supporting Information S1.

The velocity profiles along SV1, SV2, and the flume-average are very similar for each flow, with velocities increasing exponentially toward the free surface from near-zero at the base (Figure 4a). The near-zero velocities at

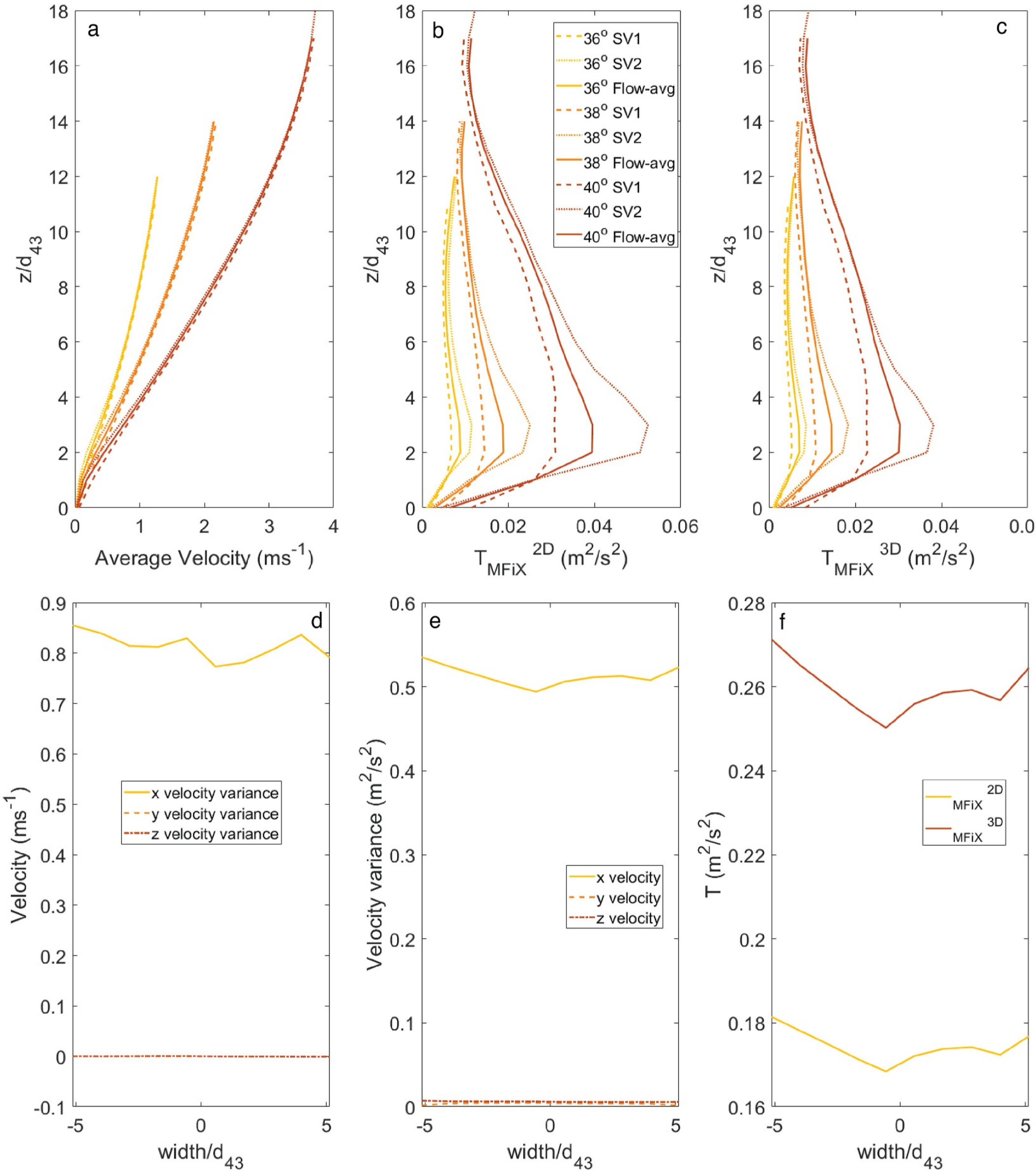

Figure 4. Numerical simulation results of granular flow dynamics for three slope inclinations (different colors). Lines with different dash styles represent measurements from either side of the simulated flow (SV1 and SV2) and from the flow-averaged profiles that include all particles. (a) Time-averaged flow-parallel velocity profiles; (b) granular temperature calculated using the two-dimensional (*x*–*z*) velocity components; (c) granular temperature calculated using all three velocity components (3D); (d) time-averaged flow-normal variance; (e) velocity variance; and (f) granular temperature profiles, highlighting flow heterogeneity at a slope inclination of 36°.

the flow–substrate contact indicate negligible basal slip. At equivalent flow heights, velocity increases with slope inclination, and the profiles become more convex.

In contrast, the T profiles show considerable divergence between SV1, SV2, and the flume-averaged calculations. This heterogeneity is confirmed by the flow-normal, time-averaged profiles illustrated in Figures 4d–4f. The irregularities of the substrate, rather than boundary effects (since velocity does not decrease near the walls), are responsible for the divergence observed between the two sides of the flow. The T profiles are non-monotonic: T increases linearly from the base, reaches a maximum near the lower region of the flow, and then decreases toward the surface (Figure 4). Although the height of this maximum varies with flow thickness, the free surfaces exhibit similar T across all inclinations. Near the free surface, the T profile becomes almost vertical. Overall, the profiles

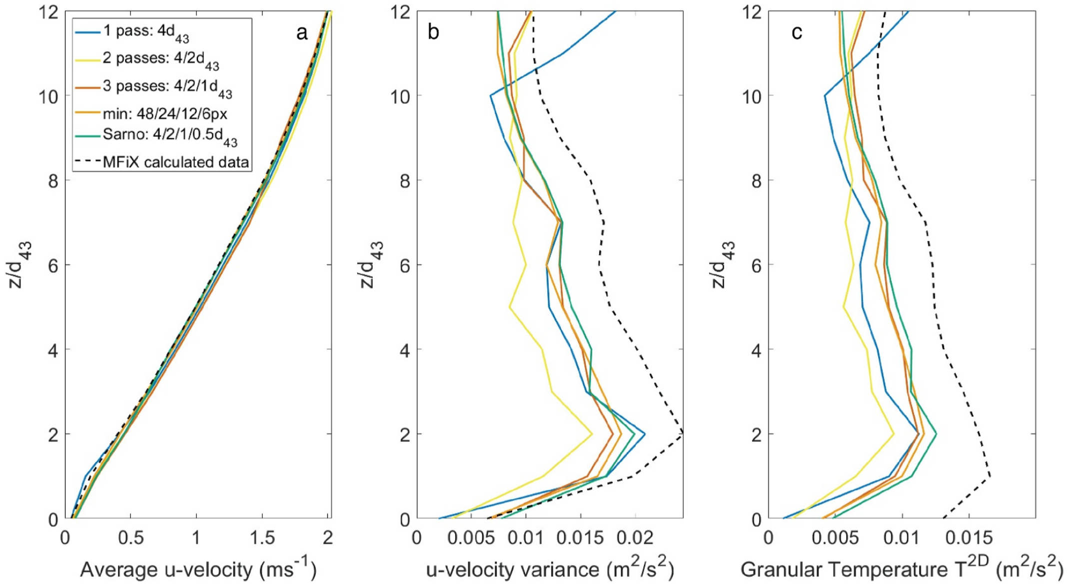

Figure 5. Influence of particle image velocimetry (PIV) configuration on measurement accuracy. Profiles represent data derived from synthetic image sequences generated from MFiX numerical simulations of granular flows at a slope inclination of 38°. Lines denote different PIV configurations, varying by the number of passes and interrogation window sizes. (a) Time averaged, flow-parallel velocity profiles; (b) velocity variance; and (c) granular temperature profiles generated using different PIV configurations on the artificial sequences.

are convex, and T is greater at equivalent flow depths for steeper slopes; the degree of convexity also increases with slope inclination. Values of $T_{\mathrm{MFiX}^{2D}}$ are consistently higher than those of $T_{\mathrm{MFiX}^{3D}}$ because the latter includes the y-component of velocity, which has lower variance (Equation 1). This distinction is discussed further in the comparison with the PIV-derived results.

3.2. PIV Calibration on the Artificial Footage

3.2.1. PIV Methodology

Different PIV parameter configurations were assessed for their precision in measuring velocity and deriving secondary statistics—variance, and T_{PIV}—by comparison with the $T_{\mathrm{MFiX}^{2D}}$ profiles calculated directly from the numerical simulations outputs. The PIV configurations employed one to four passes, with the first pass being the recommended 4 d_{43} and each subsequent pass using half the previous IW size. This included the configuration proposed by Sarno, Carravetta, et al. (2018) (4 passes at IWs of 4/2/1/0.5 d_{43}). Additionally, four passes using the minimum pixel-based recommendation were tested (four passes at areas of 48/24/12/6 pixels). All configurations produced nearly identical results for the mean velocity profiles, indicating high-precision in velocity measurements (Figure 5a). However, this consistency did not extend to the calculation of u-velocity variance and T_{PIV} (Figures 5b and 5c).

When PIV data were used to calculate variance and T_{PIV}, all configurations underestimated the true values. Despite this bias, the shape of the profiles closely matched those obtained from numerical simulations (Figures 5b and 5c). Increasing the number of passes reduced the underestimation, with the exception of the transition from 1-pass to 2-pass. The single-pass configuration produced smaller errors near the base, where velocities are low, but yielded anomalous results in the upper regions of higher velocity due to loss-of-pair errors. The profiles generated using three passes, the configuration of Sarno, Carravetta, et al. (2018), and the setup with the minimum recommended interrogation-window (IW) sizes were all very similar. However, the IW configuration of Sarno, Carravetta, et al. (2018) resulted in the least underestimation, while the minimum-IW configuration produced slightly larger errors in both variance and T_{PIV}. Therefore, following Sarno, Carravetta, et al. (2018), a four-pass configuration with IW sizes of >4/2/1/0.5d_{43} was adopted for all subsequent analyses. To minimize loss-of-pair errors, the first (largest) IW was required to have a minimum width of 4d_{43}, consistent with the earlier

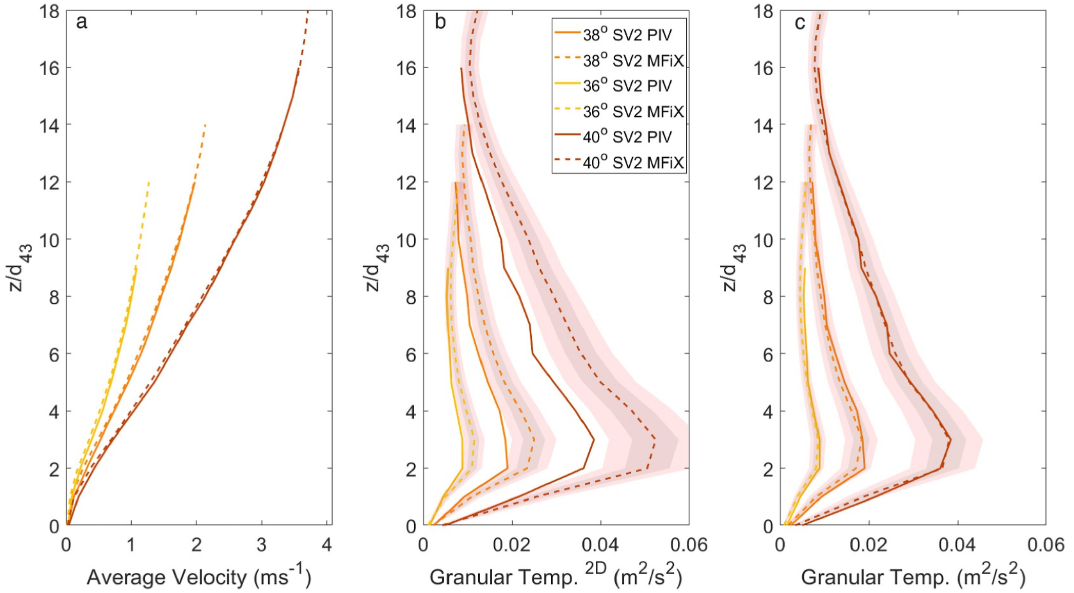

Figure 6. Comparison between discrete element method numerical simulation (MFiX) outputs and particle image velocimetry (PIV)-derived measurements: SV2 time averaged (a) velocity profiles, (b) T^{2D} profiles, and (c) T^{3D} profile comparison between $T_{\text{MFiX}^{3D}}$ calculated with all three components of the velocity of particles, while the T_{PIV} measurements only take into consideration the *x* and *z* components (2D) that can be monitored through the side wall. The gray shaded area represents a 10% margin around the MFiX measurements, and the red area 20%.

recommendation. For higher slope angles however, the initial IW had to be enlarged to track faster particles: $5d_{43}$ for 38° and $6d_{43}$ for 40° flows. The sizes of the three smaller IWs were kept constant at 2, 1, and $0.5d_{43}$.

3.2.2. PIV on Synthetic Image Sequences

A comparison between the velocity and *T* profiles measured with MFiX and PIV on the simulated image sequences is illustrated in Figure 6.

PIV applied on the MFiX output image sequences was successful at measuring the average velocity profiles of all flows, as illustrated in Figure 6a, as well as the correlation between the simulation and PIV measurements in Figure 7a. Figure 7a shows a strong correlation between velocity_{MFiX} and velocity_{PIV} ($\text{velocity}_{MFiX} = 0.994$

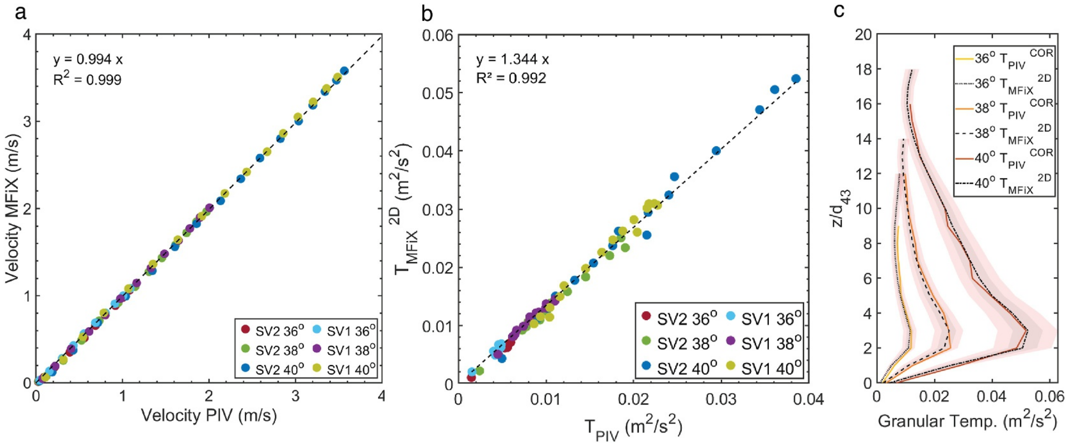

Figure 7. Correlation between numerical (MFiX) and particle image velocimetry (PIV) measurements from synthetic footage: (a) Correlation between the velocities measured in MFiX and with PIV on the artificial footage. (b) Granular temperature MFiX Vs PIV. (c) Granular temperature corrected according to the factor calculated from the comparison between MFiX-derived calculations of the granular temperature and those derived by PIV on the artificial footage generated.

velocity$_{PIV}$; $R^2 = 0.999$), based on all flow height intervals across all flows. There is an 88.61% confidence that any point falls within 10% of the best-fit line.

However, when comparing T_{PIV} to $T_{\mathrm{MFiX^{2D}}}$ in Figure 6b, PIV systematically underestimates T (Figure 6b). By contrast, when comparing T_{PIV} to $T_{\mathrm{MFiX^{3D}}}$ there is a very close match between the two (Figure 6c). This agreement is likely coincidental and specific to the simulated flows analyzed here. The PIV tracking method captures motion only in the x–z plane and thus omits the y-component of velocity. The apparent correspondence probably arises because the y-component velocities in these simulations are relatively small and contribute little to the total T. This agreement should not be interpreted as validation of PIV's ability to recover three-dimensional T. Despite this limitation, PIV consistently reproduced the shape of T profiles, correctly identifying the distribution and zones of higher T. In three out of six flows (Text S4 in Supporting Information S1), PIV correctly identified the height interval where the maximum T occurred. In the remaining three, PIV identified the adjacent interval as the location of maximum T. While PIV was precise in detecting trends and structure, it was not accurate in capturing the absolute values of T. As has been reported in previous studies, the measurements exhibit an underestimation of the velocity variance, and consequently T. By plotting T profiles from the numerical model ($T_{\mathrm{MFiX^{2D}}}$) against T_{PIV}, it is revealed that the underestimation is consistent and described by the equation $T_{\mathrm{MFiX^{2D}}} = 1.344\ T_{\mathrm{PIV}}$, with a coefficient of determination $R^2 = 0.992$ (Figure 7b). This relationship describes the measurements within a <20% error with a confidence of 96.2%, and within 10% error with a confidence of 79.75%.

The underestimation is therefore systematic and predictable, allowing correction of the PIV-derived values using the relationship described above with a factor of 1.344. The corrected T_{PIV} measurements reproduce T much more accurately, within the uncertainties noted above, as illustrated in Figure 7c.

3.3. Analog Granular Flow Experiments Analysis

3.3.1. Steady Flows Over a Fixed Rough Substrate

The numerical simulations and image sequences were designed to replicate the conditions of the analog experiments as closely as possible, ensuring that the correction factor derived from PIV analysis of the simulations would be applicable to the experimental data. The shape of the flume, particle sizes in the flow and substrate, and the frequency and resolution of the extracted footage (pixels per particle) are common between the two sets of conditions. Therefore, the same correction factor is applied to our analog experimental footage to correct for T underestimation.

For flows on a rough substrate (Figure 8), higher slope inclinations produced higher velocities at equivalent flow heights. Since the basal velocity is always close to zero, due to substrate roughness, this led to steeper overall velocity gradients. This is the canonical Bagnold-type profile for dense granular flow over a rough incline. T also increased with slope inclination at equivalent heights, producing steeper gradients immediately above the rough substrate, and more moderate gradients in the upper region between the substrate and the free surface. Elevated T values were also observed at the flow surface, where the particles are surrounded by fewer neighbors and can saltate more freely. The convexity of the T profiles increased with slope inclination, since the enhancement of T was more pronounced near the substrate.

3.3.2. Transient Flows Over an Erodible Substrate

Flows over an erodible substrate were less steady than those over a fixed substrate. They only achieved steady-state during short intervals at different stages of the passing flow. Although their transient nature makes direct comparison difficult, the velocity and T profiles of the flows were consistently self-similar and clearly distinct from those over a fixed substrate. Both the velocity and T profiles were concave, showing an exponential increase from a depth within the substrate up to the free surface of the flow (Figures 9a and 9e). The elevated T observed near the substrate in flows over a fixed substrate (Figure 8) was absent.

Because the flows are highly transient, the profiles shown in Figure 9a and e represent instantaneous snapshots. Time or spatially averaged calculations over broad regions would not reliably capture flow dynamics. To investigate the temporal evolution, spatio-temporal plots showing the vertical distribution of velocity and T through time were produced instead. These plots were based on data sampled from a narrow longitudinal section

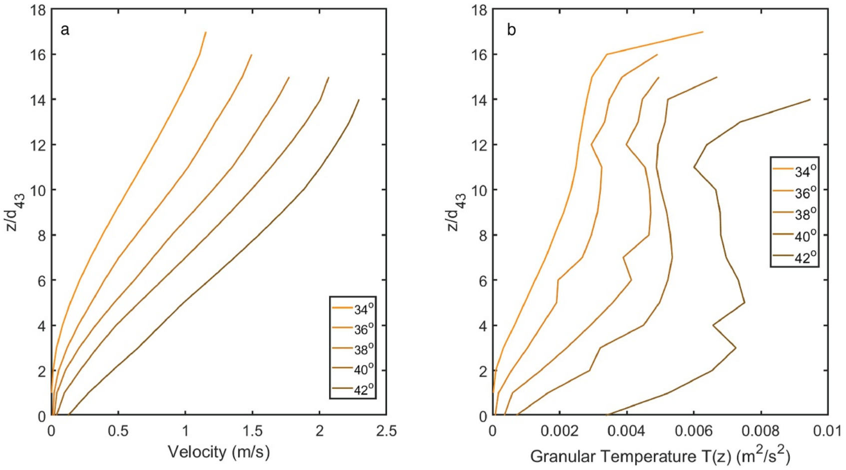

Figure 8. (a) Velocity and (b) granular temperature profiles from analog granular flow experiments conducted over a fixed rough substrate. These experiments are on a fixed rough substrate and constant supply on slope inclinations between 34° and 42°.

of the flow (23 d_{43} wide) and therefore do not represent the entire flow or longitudinal variations. The flow–substrate boundary interface was determined as described in Section 2.5 and Figure 3.

In both examples shown in Figure 9, the initial arrival of the flow front transfers momentum to the substrate, increasing its velocity. At the same time, T from the flow diffuses into the substrate as the overriding layer thickens. T is non-zero within the substrate that is not considered to be propagating and increases within the buffer zone and the flow. Some of this creeping buffer zone material subsequently re-stabilizes and becomes reclassified as part of the substrate. In addition, deposition from the overlying flow occurs, which is evident where the substrate surface rises above the previous substrate level. As material is redeposited, the substrate boundary rises toward the original level of the erodible bed, which is supported by the lip at the downstream end of the flume. Consequently, the erosion rate and its spatial distribution are transient. T reaches its highest values within the flow zone and is transmitted at lower magnitudes into the buffer zone (Figures 9d and 9h).

4. Discussion

4.1. Particle Image Velocimetry (PIV) Methodology

The PIVlab methodology proved capable of measuring time-average velocity profiles with a high accuracy (Figure 4a). The velocity profiles did not exhibit the underestimation that has often been reported. These findings indicate that time-averaged velocity measurements obtained from the portion of the flow visible through a side wall can accurately represent the overall flow field (Figure 4b) under conditions where the substrate is heterogeneous and sidewall friction is negligible. However, underestimation of the velocity variance, and consequently T_{PIV} due to spatial averaging persists, even when the smallest interrogation window (IW) is smaller than d_{43}.

Reynolds et al. (2008) used statistical arguments to illustrate that the true granular temperature (T_T) of a reference area within the flow, small enough to be comparable to a single particle, is underestimated in T_{PIV} by a factor n_R. This factor represents the ratio between the interrogation window (IW) and the reference area, with the IW being n_R times larger than the particle-scale region. In the absence of spatial correlation between adjacent instantaneous PIV measurements, they proposed:

$$T_T = n_R \times T_{PIV} \tag{5}$$

Furthermore, Reynolds et al. (2008) proposed that, in cases of full spatial correlation:

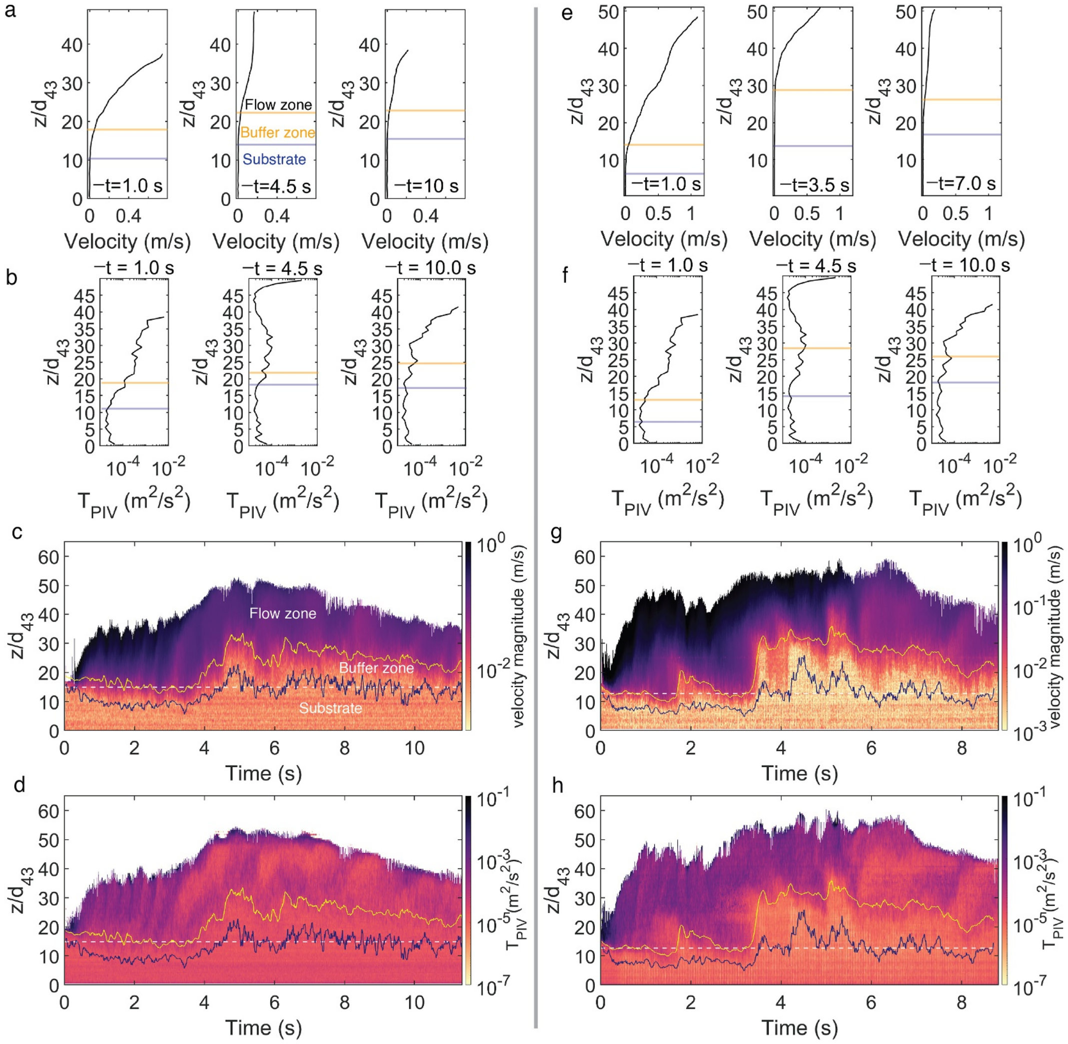

Figure 9. Spatio-temporal evolution of granular flows on an erodible substrate: (a–d) Flows generated by a gate opening of 60 mm. (a–d) Flows generated by a gate opening of 100 mm. (a, e) illustrate the transience of these flows through velocity profiles at different times; while (b, f) illustrate granular temperature profiles (logarithmic *x*-axis). (c, g) Spatio-temporal plots of the vertical distribution of velocity over time in the two flows (logarithmic colorbar). The white dashed line marks the original level of the substrate held by a lip at the end of the flume. The blue line traces the substrate of the flow, while the yellow line is describes the top of the buffer zone. (d, h) Spatio-temporal plots of the distribution of granular temperature (logarithmic colorbar).

$$T_T = T_{PIV} \tag{6}$$

and that such a state of correlation is approached on a length scale of 1 particle diameter due to the correlation of particles with themselves in consecutive frames (the statistical arguments are outlined in the supplementary material Appendix C of Sarno, Carleo, et al., 2018).

This study calculates T_{PIV} which is compared to the calculations of the T from numerical simulations, on the same flows through synthetic image sequences. Therefore, $T_{\mathrm{MFiX^{2D}}}$ calculations can be approximated as the equivalent of the T_T from the Reynolds et al. (2008) equations. Even with the two last IWs being smaller than d_{43}, the T_{PIV} is not equal to $T_{\mathrm{MFiX^{2D}}}$, even though it was theoretically predicted that the difference between the two should diminish with decreased IW size Reynolds et al. (2008). This likely reflects the inherent spatial averaging of the Eulerian PIV methodology, in which interrogation windows do not align with individual particles and therefore cannot fully resolve particle-scale correlations. Even sub-particle IWs contain pixels from neighboring grains or voids, so measured fluctuations are smoothed. Particles within one IW rarely reach velocity peaks simultaneously, either in magnitude or direction. Although the multipass configuration recommended by Sarno, Carravetta, et al. (2018) minimizes random error, it remains limited in accuracy by the inherent PIV spatial averaging. Consequently, while the measurements are precise, they are systematically biased.

In the present study, this bias is shown to be systematic across the range of velocities and T investigated, permitting the use of a single correction factor. The correction factor allows the calibration of PIV measurements and the calculation of accurate T values. This is feasible only because of the high imaging frequency and resolution, which allow IWs as small as $d_{43}/2$, while still encompassing 6–8 pixels. The correction factor is the relationship $T^{2D} = 1.344\mathrm{T}_{PIV}$ as illustrated in Figure 7b.

4.2. Limitations for the Application of the Methodology

The correction factor is a function of the ability of the PIV algorithm to identify pixel clusters within the IW (itself function of the texture of the particles (Sarno, Carravetta, et al., 2018)), the velocity of the flow in comparison to the size of the IW, and the imaging resolution and frequency. Therefore, this correction factor is likely to be valid for experimental setups with similar properties. However, experimental setups with substantial divergence from the conditions outlined in this study will potentially need to calibrate a correction factor using footage from equivalent flows, with well-constrained T. More studies will be required to evaluate whether this factor can be estimated as a function of parameters that can be quantified a priori, such as particle size or IW ratio, image resolution, and recording frequency.

Also, using PIV it is inevitable that only the particles visible from the side walls can be tracked, and only two dimensions of their velocity can be resolved. Depending on the flume width and boundary effects, the flow properties of the sampled area may not be representative of the central axis of the flow. Sidewalls can influence granular flow structure by modifying stress distributions and promoting shear localization (Jop et al., 2005). This needs to be assessed on a case-by-case basis. In this case, low friction was ensured on the walls and between all experiments the walls were sprayed with a product to reduce static charge and electrostatic effects.

Nonetheless, the uniformity of the profiles throughout the width of the flows could not be evaluated in the analog experiments. However, we evaluated the representativeness of the sidewall measurements by comparing velocity profiles obtained through the sidewall with velocity fields extracted from the full DEM-simulated flow domain (Figure 4a). Although the simulations assumed frictionless sidewalls, lateral confinement was still enforced. The DEM simulations suggest that velocity measurements might be more reliably assumed to characterize the whole of the flow compared to T, which is more variable (Figure 4) due to the variability of the substrate, rather than boundary effects. All fixed and erodible runs were conducted under identical lateral boundary conditions, the contrasting dynamics reported here are therefore attributed to basal mobility rather than sidewall confinement.

Although PIV can only resolve velocity fluctuations in two dimensions, comparison with the 3D DEM results shows that the omission of the out-of-plane component primarily affects absolute temperature magnitudes rather than the form of the profile. Nevertheless, the vertical structure and regime-diagnostic features of the T profile are robustly captured, allowing confident identification of flow behavior even where absolute values differ. Key patterns such as basal agitation over fixed beds or the smooth exponential increase of T within erodible substrates remain consistent across both 2D and 3D views, ensuring that the calibrated PIV measurements reliably reveal the underlying flow regime.

4.3. Analog Granular Flows Over Fixed Rough Substrate

The experiments suggest that, as expected, for greater flume slope inclinations the flows exhibit higher velocities at equivalent heights (Figure 8). At the steepest flume inclination of 42°, the velocity at the base is visibly above 0, enabling slip-flow behavior (Nagl et al., 2020). At lower slope inclinations, the slower flows display no basal slip and velocities are constantly near-zero at the base. This behavior is consistent with the heap flow regime described in previous studies (GDR MiDi, 2004; Jop et al., 2005, 2006; Zuccarini et al., 2025), where the higher flow velocities are confined to the higher elevations of the flow, while the base is stationary. In this regime, basal motion is inhibited by strong grain interlocking between stationary particles in the substrate and the particles in the flow. The moving grains shear over a thin, quasi-static layer of particles at the base of, and within the flow

(Jop, 2015), marking a transition from classical inclined-plane flow toward behavior more similar to flow on an erodible bed, as discussed below.

T profiles also illustrate greater values at increased slopes for equivalent flow heights. However, the profiles also become more concave, with a proportionally greater increase in *T* close to the base (Figure 8). This is the result of the particles at the base of the flow having momentum-transferring collisional interactions with the fixed particles of the substrate. This agitation propagates up and progressively diminishes away from the base of the flow toward its free upper surface. *T* increases again at the surface of the flow, where particles are less confined and more free to saltate. The distance from the base where the high basal *T* is observed decreases as the slope inclination increases. Given the greater velocity gradients near the base (i.e., greatest shear rate) it is expected that *T* is greater in that area, as also observed in Figure 8, assuming a constant solid concentration (Armanini et al., 2005; Campbell & Brennen, 1985; Sanvitale & Bowman, 2016). For the lower slope inclinations the velocity profiles in Figure 8 are more similar to flows over an erodible substrate illustrated in Figures 9a and 9e. This illustrates the fact that at these low elevations the interlocking of particles allows the accretion of a thin layer of particles at the base of the flow (since basal slip is 0). After the formation of this layer the flow is essentially propagating over a thin layer of stationary, erodible particles as in the experiments presented below. The flows presented in Figure 8 are the point of transition between the two regimes, as for the 34° flows, the stationary layer has a thickness of just one particle diameter.

4.4. Analog Granular Flows Over Erodible Substrate

The interaction between flows with an erodible substrate results in distinct velocity and *T* profiles as well as flow dynamics compared to flows over a fixed substrate. First, these flows are much more transient and are only steady for short time intervals at different stages of the flow. This is the result of the transient interaction with the substrate. The initial arrival of the flow front mobilizes particles in the substrate, increasing their velocity and *T* (Figure 9). However, as the thickness of the flow increases, the high-velocity and high-T areas migrate further from the substrate, leading material within the area of the initial substrate or even higher, to become immobilized and deposited. After the initial effect of the flow front, the flow-substrate boundary interface oscillates around the original level, supported by a lip at the end of the flume (Figure 9). This implies that at some instances the flow is mobilizing and entraining material from the substrate (bulking), but at other instances it is depositing material from the flow on top of the substrate (debulking). Observations from the footage of the flows suggest that the erosion and incorporation of material from the substrate into the flow occurs through basal abrasion (the process in which particles at the base of the flow slide parallel to particles in the substrate and mobilize them—Gauer and Issler (2004)) while bulldozing (the pushing of substrate material into mounds due to the frictional shear of the material in the propagating flow—Dufresne et al. (2010)) is also observed. The bulldozing and build-up of material and its subsequent erosion are likely the source of the transience in the flow dynamics.

The *T* and velocity profiles of flows over erodible substrates (Figures 9a, 9b, 9e, and 9f) are fundamentally different to those on a fixed substrate (Figure 8). The ability of the substrate to deform and accommodate momentum means that there is transmission of energy, momentum and *T* from the flow to the substrate. Therefore, an erodible substrate does not introduce agitation to the base of the flow by colliding and interlocking with the particles at the base. Consequently, the increased *T* observed at the base of a flow over a rough substrate is not observed. Instead, the flow transmits into the substrate. Deep in the substrate, at the base of the flume, particles do not experience any motion (substrate). At some depth the particles are moving with an exponential velocity profile (buffer zone), and further up in the flow zone the profile depends on the conditions of the flow at any given time. Therefore, velocity profiles acquire some velocity over 0 at some depth within the substrate and increase toward the free surface of the flow (Figure 9).

The fluctuating flow boundary is an important observation regarding the dynamics of geophysical granular flows which is consistent with the flow-boundary zone concept developed for pyroclastic density currents (e.g., Branney & Kokelaar, 2002). The observed transience has direct implications for interpreting basal contacts and flow–substrate interactions in field studies as it recognizes that currents can alternate between erosional and depositional states during a single event, producing complex deposit architectures. Field studies, including those on Tenerife ignimbrite by Brown and Branney (2013) and more recent work by Walding et al. (2025), demonstrate that preserved basal contacts do not necessarily represent a persistent shear surface, which has also been observed in the analog experiments (e.g., Rowley et al., 2025). These more complex geophysical flows also suggest that, unlike these experiments, maximum scour may occur during climactic phases rather than at the flow front. This is potentially due to the non-uniform discharge of such events compared to the experiments presented here. In the case of flank collapses, Makris, Roverato, Dávila-Harris et al. (2023) have observed that, at the basal boundary of the Abona volcanic debris avalanche (VDA), a pre-existing layer of thin soil is preserved in some places, while in other proximal areas is eroded by the flow. This might be an indication that the granular behavior described above was in action at the base of the flow; and it propagated over a mechanically weak erodible substrate of pumice and loose soil. The variable erosion and transience of the flow resulted in non-uniform preservation of the substrate. Evidence of bulldozing is also preserved in the substrate below the deposit (Makris, Roverato, Dávila-Harris et al., 2023).

The contact preserved between a deposit and its substrate should not be assumed to have been the active basal boundary throughout an event. In cases analogous to our experiments, the preserved boundary most likely records the maximum scour depth attained during peak forcing, likely at the arrival of the front. As the flow debulks, the active base migrates upward and aggradation resumes. Our frame-by-frame measurements show oscillation of the flow–substrate interface about the initial buttressed level, with alternating abrasion-driven erosion and bulldozing followed by deposition. Accordingly, a single preserved contact depth cannot be used to infer average erosion rates or steady basal conditions. This behavior cautions against spatially uniform or monotonic entrainment laws in depth-averaged models and underscores the need to accommodate alternating erosion and deposition when interpreting natural deposits (Calder et al., 2000; Sparks et al., 1997). These observations do allow the examination of the flow-substrate interface processes and the transience, however, it is inevitable that more complex geophysical flows will result in more complex interactions.

This sensitivity of flow dynamics to substrate erodibility parallels findings in aeolian sediment transport, where fixed and mobile beds produce distinct velocity profiles and momentum exchange (Ho et al., 2011; Kamath et al., 2022). In aeolian systems, substrate erodibility governs grain–fluid coupling and transport scaling; in the dense granular flows examined here, it controls the partitioning of velocity and granular temperature across the flow–substrate interface. In both cases, the erodibility of the boundary regulates how kinetic energy is redistributed between moving and stationary grains, fundamentally altering entrainment dynamics.

It is important to note that in the experiments over a rough substrate, illustrated in Figure 8, at the 34°, 36°, and 38° flume inclinations, the velocity profiles present form analogous to the erodible substrate because the flow is able to deposit its own substrate, to some degree. At these shallow slopes, as particles at the base have near-zero velocities (importantly, in the case of erodible substrate they are truly deposited with no granular temperature), whereas at the steeper inclinations there is no part of the flow that is not moving. Once a layer of particles is deposited at the base, the flow stops interfering with the rough substrate and instead behaves as a flow over an erodible substrate.

The present study provides observations of these dynamics and a mechanistic explanation for how such transience arises in simple dense granular systems. By resolving velocity and T across fixed and erodible substrates, we show how agitation is transmitted, how the flow–substrate boundary oscillates along with erosion and deposition. The method developed here allows the quantitative observation and tracking of the flow-substrate boundary. These observations demonstrate the transience that even laboratory flows exhibit, reinforcing the need to interpret preserved basal contacts in natural deposits as dynamic records of evolving flow–boundary interactions.

The transient erosion and deposition patterns observed in the experiments (Figure 9) are important for understanding and modeling granular flow dynamics. For instance, the bulking and debulking terms used in depth-averaged numerical simulations of pyroclastic density currents rely on parameters such as flow thickness and temporal velocity gradient. In these models, this prediction is critical because the eroded or deposited material is incorporated or lost, therefore impacting the mass and momentum of the bulk flow. As illustrated in Figure 10, the bulking and debulking formulations proposed by Bernard et al. (2014) and Fagents and Baloga (2006) were applied to predict erosion/deposition patterns and compared with the experimental measurements. The erosion rate ($\frac{\partial h}{\partial t}$ ms^{-1}) in Bernard et al. (2014) is expressed as:

$$\frac{\partial h}{\partial t} = \frac{d_{43}}{t_{er}} \tag{7}$$

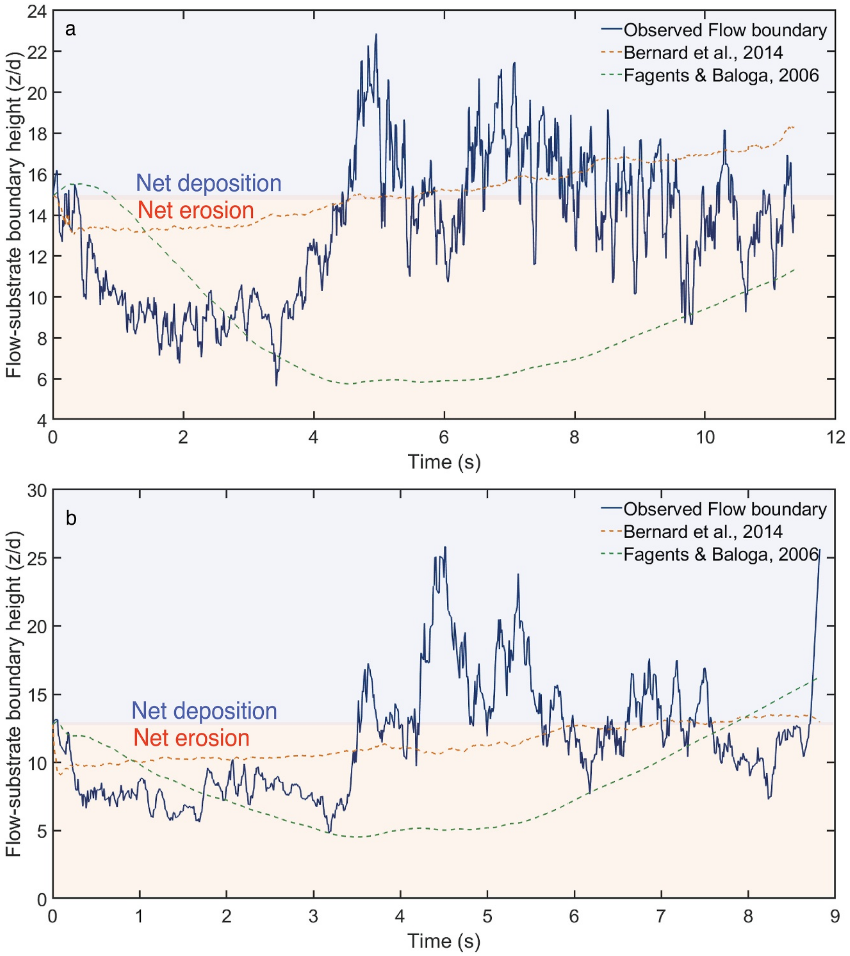

Figure 10. Comparison between the observed flow-substrate boundary level within the substrate (solid blue line), and the same level as predicted by different bulking/debulking terms proposed in the literature (dotted colored lines). The data are from experiments with an erodible substrate at 31.5° and (a) 60 mm gate opening (b) 100 mm gate opening.

as the height of the flow (h) changes over time (t). The total erosion time t_{er} is defined as:

$$t_{er} = \frac{m}{F} \times v_f + \frac{d_{43} - D}{v_f} \tag{8}$$

and the sum of external forces on a particle (F) as:

$$F = m\frac{\partial v_f}{\partial t} \tag{9}$$

m is the mass of a particle (kg), v_f (ms^{-1}) is the velocity of the flow and D (m) is the distance traveled by an entrained particle in a defined time interval.

In Fagents and Baloga (2006) the erosion rate is estimated as:

$$\frac{\partial h}{\partial t} = \varepsilon(x)B + (1 - \varepsilon(x))D - \frac{\partial}{\partial x}(hv_f) \tag{10}$$

where the bulking (B ms^{-1}) term is defined as:

$$B = \lambda v_f h \left[\frac{\rho_{\max} - \rho}{\rho_{\max} - \rho_0} \right] \tag{11}$$

and the debulking term (D ms^{-1}) is defined as:

$$D = -v_s \left[\frac{\rho - \rho_{air}}{\rho_s - \rho_{air}} \right] \tag{12}$$

λ (ms^{-1}) is an entrainment parameter ($\lambda = 1.8\ \mathrm{ms}^{-1}$ for 60 mm gate opening in Figure 10a, $\lambda = 0.95$ for 100 mm gate opening in Figure 10b), v_s (ms^{-1}) is a theoretical settling velocity of the sediment employed as a debulking parameter ($v_s = 0.004$ for 60 mm gate opening in Figure 10a, $v_s = 0.008$ for 100 mm gate opening in Figure 10b), ρ (kgm^{-3}) is the bulk density of the granular material used in the experiments (=1,475.49 kgm^{-3}), ρ_s is the solid density of the sand used in the experiments (=2,500.00 kgm^{-3}), $\rho_{\max}$ is the maximum flow density (=1,600.43 kgm^{-3}), ρ_0 is the flow density at source (=1,500.48 kgm^{-3}) and ρ_{air} is the density of air which composes the pore space (=1.23 kgm^{-3}). The Fermi function, $\varepsilon(x)$ (Fagents & Baloga, 2006), in 10 was constant at 0.5 to give equal weight to the bulking and debulking since the flume had a constant slope with no variation or a break of slope. The λ and v_s values were used to calibrate each of the models to the maximum erosion depth, as can be done in field studies of mass flows.

The results indicate that although the Fagents and Baloga (2006) model can approximate the maximum erosion depth, both models fail to reproduces the amplitude of the transient erosion pattern or the corresponding variations in substrate depth and flow thickness through time (Figure 10). The Bernard et al. (2014) formulation underestimates the magnitude of these oscillations and consequently the variations in flow-substrate boundary depth and flow volume. In contrast, the Fagents and Baloga (2006) model captures the initial erosion produced by the flow front but fails to represent the subsequent rapid deposition and oscillatory motion of the flow–substrate interface.

Flows where grains from the bed can become entrained, exhibit lower basal particle agitation than flows over non-erodible beds. This reduction arises from enhanced momentum exchange, as entrained substrate material contributes mass and momentum to the flow front, increasing overall mobility. This behavior agrees with field observations of debris flows and snow avalanches, where basal entrainment increases flow mass, extends runout, and lowers effective basal friction (Iverson & Ouyang, 2015; Li et al., 2024; Pudasaini & Krautblatter, 2021). For instance, snow avalanches can undergo dramatic shifts in behavior when basal snow is entrained, greatly amplifying their destructive potential (Pudasaini & Krautblatter, 2022).

These findings are consistent with extended kinetic-theory models that incorporate erodible beds and explicitly describe momentum and energy transfer at the flow–substrate interface (Berzi et al., 2020; Jenkins & Berzi, 2016). Incorporating realistic basal boundary conditions is therefore essential for both experimental design and numerical modeling. In particular, boundary conditions informed by extended kinetic theory, capable of capturing material exchange and T evolution, are key to simulating geophysical granular flows and improving predictions of hazards such as rock and snow avalanches (Capart, 2023; Jenkins & Berzi, 2016; Jenkins et al., 2020).

5. Conclusions

This study evaluates the accuracy of PIV for measuring velocity and granular temperature (T) in free-surface granular flows, using analog experiments and DEM simulations. PIV accurately recovers time-averaged velocity profiles but systematically underestimates T due to Eulerian spatial averaging within interrogation windows. Applying PIV to synthetic sequences derived from simulations with particle-resolved kinematics shows that the underestimation of T persists even with multi-pass PIV and sub-particle interrogation windows. The bias is uniform across the conditions tested and can be corrected with a single empirical factor of ∼1.34, as calculated by comparing numerical simulation and PIV-derived T values. Despite these improvements, some limitations remain. The correction factor is derived under controlled conditions and may vary with particle size, shape, and imaging resolution. Additionally, PIV only captures velocity fluctuations in two dimensions, meaning that estimates of T do not account for out-of-plane velocity components.

The calibrated workflow allows the quantitative examination of flow dynamics and the flow-substrate boundary. It enables frame-by-frame localization of the flow–substrate boundary and quantification of evolving erosion–deposition patterns. Flows over erodible beds exhibit velocity and T structures that differ fundamentally from flows over fixed rough beds. An erodible bed accommodates momentum, so energy and agitation are dissipated into the substrate rather than being generated by collisions with immobile substrate particles. As a result, velocities become non-zero within the erodible substrate and increase toward the free surface, and the basal T spike that characterizes fixed-bed runs is absent. Using our classification, enabled by the accurate tracking of particle velocities, velocity profiles are partitioned into a stationary substrate zone, an exponentially shearing buffer zone, and an overlying flow zone. On fixed beds at shallow slopes (34°–38°), a thin quasi-static basal layer can develop, causing velocity profiles that resemble those over erodible beds. At steeper slopes the entire depth remains mobile. Over erodible beds the flow–substrate interface oscillates through time, with alternating abrasion-driven erosion, bulldozing, and deposition. Consequently, a single preserved basal contact in the deposit typically records a maximum scour depth. This is in agreement with field studies interpreting a dynamic flow-substrate interface, however in this simple experiments it can be located, observed and quantified with the workflow developed. These observations caution against spatially uniform or monotonic entrainment laws in depth-averaged models and motivate formulations that accommodate alternating erosion and deposition and time-variant basal conditions.

Overall, this study provides a practical calibration to validate velocity measurements and improve the recovery of T from PIV. Furthermore, it reveals transient basal dynamics in erodible beds that are essential for evaluating substrate entrainment closures and to interpret preserved contacts in geophysical granular-flow deposits.

Conflict of Interest

The authors declare no conflicts of interest relevant to this study.

Availability Statement

Examples of the data which supports the described results and allows their reproduction are available on the open-access repository *Zenodo* at https://doi.org/10.5281/zenodo.17572865 (Makris, 2025). This includes videos of the flows, scaling information, and flow stability evaluations. Discrete element method (DEM) numerical simulations were carried out with the MFiX open-source code developed by the US Department of Energy's National Energy Technology Laboratory (NETL) (Syamlal et al., 2016) which can be accessed at https://mfix.netl.doe.gov. Photogrammetry was carried out using the open-source *PIVlab* code Thielicke and Stamhuis (2014), Thielicke and Stamhuis (2019).

Acknowledgments
The authors would like to thank Professor Eric Parteli, two anonymous reviewers and Dr Matt Arran (BGS) for their in-depth review and comments that considerably improved this paper. This was work was supported by the NERC Standard Grant (NE/R011001/1) awarded to E.S.C. E.C.P. B. was supported by the NERC-IRF (NE/V014242/1), the Leverhulme Trust grant award RPG-2024-294 and the Royal Society (IEC/NSFC/242381) and acknowledges the use of ARCHER2 High Performance Computing. SM was supported by the BGS International NC programme "Geoscience to tackle Global Environmental Challenges," NERC reference NE/X006255/1. The paper is published by permission of the Director of the British Geological Survey (United Kingdom Research and Innovation).

References

Albaraki, S., & Antony, S. J. (2014). How does internal angle of hoppers affect granular flow? Experimental studies using digital particle image velocimetry. *Powder Technology*, *268*, 253–260. https://doi.org/10.1016/j.powtec.2014.08.027

Armanini, A., Capart, H., Fraccarollo, L., & Larcher, M. (2005). Rheological stratification in experimental free-surface flows of granular-liquid mixtures. *Journal of Fluid Mechanics*, *532*, 269–319. https://doi.org/10.1017/S0022112005004283

Arran, M. I., Mangeney, A., De Rosny, J., & Toussaint, R. (2024). Simulated slidequakes: Insights from DEM simulations into the high-frequency seismic signal generated by geophysical granular flows. *Journal of Geophysical Research: Earth Surface*, *129*(8), e2023JF007455. https://doi.org/10.1029/2023jf007455

Bagnold, R. A. (1956). The flow of cohesionless grains in fluids. *Philosophical Transactions of the Royal Society of London. Series A, Mathematical and Physical Sciences*, *249*(964), 235–297. https://doi.org/10.1098/rsta.1956.0020

Bernard, J., Kelfoun, K., Le Pennec, J.-L., & Vallejo Vargas, S. (2014). Pyroclastic flow erosion and bulking processes: Comparing field-based vs. modeling results at Tungurahua volcano, Ecuador. *Bulletin of Volcanology*, *76*(9), 858. https://doi.org/10.1007/s00445-014-0858-y

Berzi, D., Jenkins, J. T., & Richard, P. (2020). Extended kinetic theory for granular flow over and within an inclined erodible bed. *Journal of Fluid Mechanics*, *885*, A27. https://doi.org/10.1017/jfm.2019.1017

Branney, M. J., & Kokelaar, B. P. (2002). Pyroclastic density currents and the sedimentation of ignimbrites (Vol. *27*, p. 37–49). https://doi.org/10.1144/GSL.MEM.2003.027.01.04

Breard, E. C., Dufek, J., Fullard, L., & Carrara, A. (2020). The basal friction coefficient of granular flows with and without excess pore pressure: Implications for pyroclastic density currents, water-rich debris flows, and rock and submarine avalanches. *Journal of Geophysical Research: Solid Earth*, *125*(12), e2020JB020203. https://doi.org/10.1029/2020jb020203

Breard, E. C., Fullard, L., & Dufek, J. (2024). Rheology of granular mixtures with varying size, density, particle friction, and flow geometry. *Physical Review Fluids*, *9*(5), 054303. https://doi.org/10.1103/physrevfluids.9.054303

Breard, E. C., Jones, J. R., Fullard, L., Lube, G., Davies, C., & Dufek, J. (2019). The permeability of volcanic mixtures—Implications for pyroclastic currents. *Journal of Geophysical Research: Solid Earth*, *124*(2), 1343–1360. https://doi.org/10.1029/2018jb016544

Brilliantov, N. V., & Pöschel, T. (2004). *Kinetic theory of granular gases*. Oxford University Press.

Brilliantov, N. V., & Pöschel, T. (2010). *Kinetic theory of granular gases*. Oxford University Press.

Brown, R. J., & Branney, M. J. (2013). Internal flow variations and diachronous sedimentation within extensive, sustained, density-stratified pyroclastic density currents flowing down gentle slopes, as revealed by the internal architectures of ignimbrites on tenerife. *Bulletin of Volcanology*, *75*(7), 727. https://doi.org/10.1007/s00445-013-0727-0

Calder, E., Sparks, R., & Gardeweg, M. (2000). Erosion, transport and segregation of pumice and lithic clasts in pyroclastic flows inferred from ignimbrite at Lascar Volcano, Chile. *Journal of Volcanology and Geothermal Research*, *104*(1–4), 201–235. https://doi.org/10.1016/s0377-0273(00)00207-9

Campbell, C. S. (1990). Rapid granular flows. *Annual Review of Fluid Mechanics*, *22*(1), 57–90. https://doi.org/10.1146/annurev.fl.22.010190.000421

Campbell, C. S. (2005). Stress-controlled elastic granular shear flows. *Journal of Fluid Mechanics*, *539*, 273–297. https://doi.org/10.1017/S0022112005005616

Campbell, C. S., & Brennen, C. E. (1985). Chute flows of granular material: Some computer simulations. *Journal of Applied Mechanics*, *52*(1), 172–178. https://doi.org/10.1115/1.3168990

Capart, H. (2023). Basal boundary conditions for granular surface flows over fragile and brittle erodible beds. *Journal of Fluid Mechanics*, *957*, A26. https://doi.org/10.1017/jfm.2023.65

Crassous, J., Metayer, J.-F., Richard, P., & Laroche, C. (2008). Experimental study of a creeping granular flow at very low velocity. *Journal of Statistical Mechanics: Theory and Experiment*, *2008*(3), P03009. https://doi.org/10.1088/1742-5468/2008/03/p03009

Cundall, P. A., & Strack, O. D. (1979). A discrete numerical model for granular assemblies. *Géotechnique*, *29*(1), 47–65. https://doi.org/10.1680/geot.1979.29.1.47

Drake, T. G. (1991). Granular flow: Physical experiments and their implications for microstructural theories. *Journal of Fluid Mechanics*, *225*, 121–152. https://doi.org/10.1017/S0022112091001994

Dufresne, A., Davies, T., & McSaveney, M. (2010). Influence of runout-path material on emplacement of the round top rock avalanche, New Zealand. *Earth Surface Processes and Landforms: The Journal of the British Geomorphological Research Group*, *35*(2), 190–201. https://doi.org/10.1002/esp.1900

Eckart, W., Gray, J. M. N. T., & Hutter, K. (2003). Particle image velocimetry (piv) for granular avalanches on inclined planes. In K. Hutter & N. Kirchner (Eds.), *Dynamic response of granular and porous materials under large and catastrophic deformations* (pp. 195–218). Springer Berlin Heidelberg. https://doi.org/10.1007/978-3-540-36565-5_6

Fagents, S. A., & Baloga, S. M. (2006). Toward a model for the bulking and debulking of lahars. *Journal of Geophysical Research*, *111*(B10). https://doi.org/10.1029/2005jb003986

Gauer, P., & Issler, D. (2004). Possible erosion mechanisms in snow avalanches. *Annals of Glaciology*, *38*, 384–392. https://doi.org/10.3189/172756404781815068

GDR MiDi, G. (2004). On dense granular flows. *European Physical Journal E: Soft Matter*, *14*(4), 341–365. https://doi.org/10.1140/epje/i2003-10153-0

Gollin, D., Brevis, W., Bowman, E. T., & Shepley, P. (2017). Performance of piv and ptv for granular flow measurements. *Granular Matter*, *19*(3), 1–16. https://doi.org/10.1007/s10035-017-0730-9

Gu, Y., Ozel, A., & Sundaresan, S. (2016). Rheology of granular materials with size distributions across dense-flow regimes. *Powder Technology*, *295*, 322–329. https://doi.org/10.1016/j.powtec.2016.03.035

Ho, T. D., Valance, A., Dupont, P., & Ould El Moctar, A. (2011). Scaling laws in aeolian sand transport. *Physical Review Letters*, *106*(9), 094501. https://doi.org/10.1103/PhysRevLett.106.094501

Iverson, R. M. (1997). The physics of debris flows. *Reviews of Geophysics*, *35*(3), 245–296. https://doi.org/10.1029/97RG00426

Iverson, R. M., & Ouyang, C. (2015). Entrainment of bed material by earth-surface mass flows: Review and reformulation of depth-integrated theory. *Reviews of Geophysics*, *53*(1), 27–58. https://doi.org/10.1002/2013rg000447

Iverson, R. M., & Vallance, J. W. (2001). New views of granular mass flows. *Geology*, *29*(2), 115–118. https://doi.org/10.1130/0091-7613(2001)029<0115:nvogmf>2.0.co;2

Jenkins, J. T., & Berzi, D. (2016). Erosion and deposition in depth-averaged models of dense, dry, inclined granular flows. *Physical Review E*, *94*(5), 052904. https://doi.org/10.1103/physreve.94.052904

Jenkins, J. T., Berzi, D., & Richard, P. (2020). Granular flows over erodible beds: Extended kinetic theory formulations. *Journal of Fluid Mechanics*, *885*, A27. https://doi.org/10.1017/jfm.2019.1017

Jerolmack, D. J., & Daniels, K. E. (2019). Viewing earth's surface as a soft-matter landscape. *Nature Reviews Physics*, *1*(12), 716–730. https://doi.org/10.1038/s42254-019-0111-x

Jesuthasan, N., Baliga, B. R., & Savage, S. B. (2006). Use of particle tracking velocimetry for measurements of granular flows: Review and application—Particle tracking velocimetry for granular flow measurements. *KONA Powder and Particle Journal*, *24*, 15–26. https://doi.org/10.14356/kona.2006006

Jiang, Y.-J., & Towhata, I. (2013). Experimental study of dry granular flow and impact behavior against a rigid retaining wall. *Rock Mechanics and Rock Engineering*, *46*(4), 713–729. https://doi.org/10.1007/s00603-012-0293-3

Johnson, B. C., Campbell, C. S., & Melosh, H. J. (2016). The reduction of friction in long runout landslides as an emergent phenomenon. *Journal of Geophysical Research: Earth Surface*, *121*(5), 881–889. https://doi.org/10.1002/2015jf003751

Jop, P. (2015). Rheological properties of dense granular flows. *Comptes Rendus Physique*, *16*(1), 62–72. https://doi.org/10.1016/j.crhy.2014.12.001

Jop, P., Forterre, Y., & Pouliquen, O. (2005). Crucial role of sidewalls in granular surface flows: Consequences for the rheology. *Journal of Fluid Mechanics*, *541*, 167–192. https://doi.org/10.1017/s0022112005005987

Jop, P., Forterre, Y., & Pouliquen, O. (2006). A constitutive law for dense granular flows. *Nature*, *441*(7094), 727–730. https://doi.org/10.1038/nature04801

Kamath, S., Shao, Y., & Parteli, E. J. (2022). Scaling laws in aeolian sand transport under low sand availability. *Geophysical Research Letters*, *49*(11), e2022GL097767. https://doi.org/10.1029/2022gl097767

Keane, R. D., & Adrian, R. J. (1990). Optimization of particle image velocimeters. I. Double pulsed systems. *Measurement Science and Technology*, *1*(11), 1202–1215. https://doi.org/10.1088/0957-0233/1/11/013

Keane, R. D., & Adrian, R. J. (1992). Theory of cross-correlation analysis of PIV images. *Applied Scientific Research*, *49*(3), 191–215. https://doi.org/10.1007/bf00384623

Kim, S., & Kamrin, K. (2020). Power-law scaling in granular rheology across flow geometries. *Physical Review Letters*, *125*(8), 088002. https://doi.org/10.1103/physrevlett.125.088002

Komatsu, T. S., Inagaki, S., Nakagawa, N., & Nasuno, S. (2001). Creep motion in a granular pile exhibiting steady surface flow. *Physical Review Letters*, *86*(9), 1757–1760. https://doi.org/10.1103/physrevlett.86.1757

Li, X., Sovilla, B., Gray, J. M. N. T., & Gaume, J. (2024). Transient wave activity in snow avalanches is controlled by entrainment and topography. *Communications Earth and Environment*, *5*(1), 77. https://doi.org/10.1038/s43247-023-01157-x

Makris, S. (2025). Calibrated granular-flow PIV from DEM simulations: Insights into experimental granular flows with fixed and erodible substrates, modelling and field implications [DATA REPOSITORY]. *Zenodo*. https://doi.org/10.5281/zenodo.17572865

Makris, S., Manzella, I., & Sgarabotto, A. (2024). Scale-dependent processes and runout in bidisperse granular flows: Insights from laboratory experiments and implications for rock/debris avalanches. *Journal of Geophysical Research: Earth Surface*, *129*(9), e2023JF007469. https://doi.org/10.1029/2023jf007469

Makris, S., Roverato, M., Dávila-Harris, P., Cole, P., & Manzella, I. (2023). Distributed stress fluidisation: Insights into the propagation mechanisms of the abona volcanic debris avalanche (Tenerife) through a novel method for indurated deposit sedimentological analysis. *Frontiers in Earth Science*, *11*, 1177507. https://doi.org/10.3389/feart.2023.1177507

Makris, S., Roverato, M., Lomoschitz, A., Cole, P., & Manzella, I. (2023). The propagation and emplacement mechanisms of the tenteniguada volcanic debris avalanche (gran canaria): Field evidence for brittle fault-accommodated spreading. *Journal of Volcanology and Geothermal Research*, *435*, 107773. https://doi.org/10.1016/j.jvolgeores.2023.107773

Nagl, G., Hübl, J., & Kaitna, R. (2020). Velocity profiles and basal stresses in natural debris flows. *Earth Surface Processes and Landforms*, *45*(8), 1764–1776. https://doi.org/10.1002/esp.4844

Ogawa, S. (1978). Multitemperature theory of granular materials. In *Proceedings of the US-Japan seminar on continuum mechanical and statistical approaches in the mechanics of granular materials* (pp. 208–217). Retrieved from https://cir.nii.ac.jp/crid/1570854175911130624

Ostendorf, M., & Schwedes, J. (2005). Application of particle image velocimetry for velocity measurements during silo discharge. *Powder Technology*, *158*(1–3), 69–75. https://doi.org/10.1016/j.powtec.2005.04.020

O'Sullivan, C. (2011). *Particulate discrete element modelling: A geomechanics perspective*. CRC Press.

Pähtz, T., & Durán, O. (2020). Unification of aeolian and fluvial sediment transport rate from granular physics. *Physical Review Letters*, *124*(16), 168001. https://doi.org/10.1103/PhysRevLett.124.168001

Pudasaini, S. P., & Krautblatter, M. (2022). Different erosion and entrainment mechanisms in snow avalanches. *Cold Regions Science and Technology*, *201*, 103592. https://doi.org/10.1016/j.mechrescom.2022.103914

Pudasaini, S. P., & Krautblatter, M. (2021). The mechanics of landslide mobility with erosion. *Nature Communications*, *12*(1), 6793. https://doi.org/10.1038/s41467-021-26959-5

Raffel, M., Willert, C. E., Wereley, S. T., & Kompenhans, J. (2007). *Particle image velocimetry: A practical guide* (2nd ed.). Springer. https://doi.org/10.1007/978-3-540-72308-0

Reynolds, G. K., Nilpawar, A. M., Salman, A. D., & Hounslow, M. J. (2008). Direct measurement of surface granular temperature in a high shear granulator. *Powder Technology*, *182*(2), 211–217. https://doi.org/10.1016/j.powtec.2007.11.034

Richard, P., Artoni, R., Valance, A., & Delannay, R. (2020). Influence of lateral confinement on granular flows: Comparison between shear-driven and gravity-driven flows. *Granular Matter*, *22*(4), 1–13. https://doi.org/10.1007/s10035-020-01057-3

Rowley, P., Williams, R., Johnson, M., Johnston, T., Dowey, N., Parsons, D., et al. (2025). Spontaneous unsteadiness and sorting in pyroclastic density currents and their deposits. In *Particulate gravity currents* (pp. 249–266). American Geophysical Union (AGU). https://doi.org/10.1002/9781394216727.ch16

Sanvitale, N., & Bowman, E. T. (2016). Using PIV to measure granular temperature in saturated unsteady polydisperse granular flows. *Granular Matter*, *18*(3), 1–12. https://doi.org/10.1007/s10035-016-0620-6

Sarno, L., Carleo, L., Papa, M. N., & Villani, P. (2018). Experimental investigation on the effects of the fixed boundaries in channelized dry granular flows. *Rock Mechanics and Rock Engineering*, *51*(1), 203–225. https://doi.org/10.1007/s00603-017-1311-2

Sarno, L., Carravetta, A., Tai, Y.-C., Papa, M., & Kuo, C.-Y. (2018). Measuring the velocity fields of granular flows—Employment of a multi-pass two-dimensional particle image velocimetry (2D-PIV) approach. *Advanced Powder Technology*, *29*(12), 3107–3123. https://doi.org/10.1016/j.apt.2018.08.014

Sielamowicz, I., Czech, M., & Kowalewski, T. A. (2011). Empirical analysis of eccentric flow registered by the DPIV technique inside a silo model. *Powder Technology*, *212*(1), 38–56. https://doi.org/10.1016/j.powtec.2011.04.022

Sparks, R., Gardeweg, M., Calder, E., & Matthews, S. (1997). Erosion by pyroclastic flows on Lascar Volcano, Chile. *Bulletin of Volcanology*, *58*(7), 557–565. https://doi.org/10.1007/s004450050162

Straub, S. (1996). Self-organization in the rapid flow of granular material: Evidence for a major flow mechanism. *Geologische Rundschau*, *85*(1), 85–91. https://doi.org/10.1007/s005310050055

Syamlal, M., Musser, J., & Dietiker, J.-F. (2016). Two-fluid model in MFIX [Software]. *Multiphase flow handbook*, 242–274. https://mfix.netl.doe.gov/doc/mfix/21.4/html/reference/two_fluid_model.html

Tai, Y.-C., & Kuo, C.-Y. (2008). A new model of granular flows over general topography with erosion and deposition. *Acta Mechanica*, *199*(1–4), 71–96. https://doi.org/10.1007/s00707-007-0560-7

Taylor-Noonan, A., Gollin, D., Bowman, E., & Take, W. (2021). The influence of image analysis methodology on the calculation of granular temperature for granular flows. *Granular Matter*, *23*(4), 96. https://doi.org/10.1007/s10035-021-01153-y

Thielicke, W., & Sonntag, R. (2021). Particle image velocimetry for MATLAB: Accuracy and enhanced algorithms in PIVlab. *Journal of Open Research Software*, *9*(1), 12. https://doi.org/10.5334/jors.334

Thielicke, W., & Stamhuis, E. J. (2014). PIVlab—Towards user-friendly, affordable and accurate digital particle image velocimetry in MATLAB [Software]. *Journal of Open Research Software*, *2*, 30. https://doi.org/10.5334/jors.bl

Thielicke, W., & Stamhuis, E. J. (2019). PIVlab—Time-Resolved digital particle image velocimetry tool for MATLAB [Software]. *Online resource*. https://doi.org/10.6084/m9.figshare.1092508.v19

Walding, N., Williams, R., Dowey, N., Rowley, P., Thomas, M., Osman, S., et al. (2025). The influence of moisture on ash strength: Implications for understanding volcanic stratigraphy. *Bulletin of Volcanology*, *87*(6), 39. https://doi.org/10.1007/s00445-025-01821-4

Westerweel, J. (1993). *Digital particle image velocimetry theory and application. Ph. D. thesis*. Delft University of Technology.

Zhu, H., Zhou, Z., Yang, R., & Yu, A. (2008). Discrete particle simulation of particulate systems: A review of major applications and findings. *Chemical Engineering Science*, *63*(23), 5728–5770. https://doi.org/10.1016/j.ces.2008.08.006

Zrelak, P., Breard, E. C. P., & Dufek, J. (2024). Laboratory landquakes: Insights from experiments into the high-frequency seismic signal generated by geophysical granular flows. *Journal of Geophysical Research: Earth Surface*, *129*(8), e2024JF008015. https://doi.org/10.1002/essoar.10504150.2

Zuccarini, A., Vasu, N., Banks, V., Bowman, E., Leonardi, A., & Berti, M. (2025). PIV analysis of flow-type landslides under suboptimal image conditions. *Landslides*, *22*(7), 1–20. https://doi.org/10.1007/s10346-025-02498-8